

Discontinuous Hamiltonian Monte Carlo for discrete parameters and discontinuous likelihoods

BY AKIHIKO NISHIMURA

*Department of Biomathematics, University of California - Los Angeles,
695 Charles E Young Dr S, Los Angeles, California 90095, U.S.A.*

akihiko4@ucla.edu

DAVID B. DUNSON

*Department of Statistical Science, Duke University,
Box 90251, Durham, North Carolina 27708, U.S.A.*

dunson@duke.edu

JIANFENG LU

*Department of Mathematics, Duke University,
Box 90320, Durham, North Carolina 27708, U.S.A.*

jianfeng@math.duke.edu

SUMMARY

Hamiltonian Monte Carlo has emerged as a standard tool for posterior computation. In this article, we present an extension that can efficiently explore target distributions with discontinuous densities, which in turn enables efficient sampling from ordinal parameters through embedding of probability mass functions into continuous spaces. We motivate our approach through a theory of discontinuous Hamiltonian dynamics and develop a corresponding numerical solver. The proposed solver is the first of its kind, with a remarkable ability to *exactly* preserve the Hamiltonian and thus yield a type of *rejection-free* proposal. We apply our algorithm to challenging posterior inference problems to demonstrate its wide applicability and competitive performance.

Some key words: Bayesian inference, geometric numerical integration, Markov chain Monte Carlo, measure-valued differential equation, rejection-free

1. INTRODUCTION

Markov chain Monte Carlo is routinely used to generate samples from posterior distributions. While specialized algorithms exist for restricted model classes, general-purpose algorithms are often inefficient and scale poorly in the number of parameters. Originally proposed by Duane et al. (1987) and popularized in the statistics community through the works of Neal (1996, 2010), Hamiltonian Monte Carlo promises a better scalability (Neal, 2010; Beskos et al., 2013) and has enjoyed wide-ranging successes as one of the most reliable approaches in general settings (Gelman et al., 2013; Kruschke, 2014; Monnahan et al., 2016).

However, a fundamental limitation of Hamiltonian Monte Carlo is the lack of support for discrete parameters (Gelman et al., 2015; Monnahan et al., 2016). The difficulty stems from the fact that the construction of Hamiltonian Monte Carlo proposals relies on a numerical solution

of a differential equation. The use of a surrogate continuous target distribution may be possible in special cases (Zhang et al., 2012), but approximating a discrete parameter of a likelihood by a continuous one is difficult in general (Berger et al., 2012).

This article presents *discontinuous Hamiltonian Monte Carlo*, an extension that can efficiently explore discrete spaces involving ordinal discrete parameters as well as continuous ones. The algorithm can also handle discontinuities in otherwise piecewise smooth posterior densities, which for example arise from models with structural change points (Chib, 1998; Wagner et al., 2002), latent thresholds (Neelon & Dunson, 2004; Nakajima & West, 2013), and pseudo-likelihoods (Bissiri et al., 2016).

Discontinuous Hamiltonian Monte Carlo retains the generality that makes Hamiltonian Monte Carlo suitable for automatic posterior inference. For any given target distribution, each iteration only requires evaluations of the density and of the following quantities up to normalizing constants: 1) full conditional densities of discrete parameters, and 2) either the gradient of the log density with respect to continuous parameters or their individual full conditional densities. Evaluations of full conditionals can be done algorithmically and efficiently through directed acyclic graph frameworks, taking advantage of conditional independence structures (Lunn et al., 2009). Algorithmic evaluation of the gradient is also efficient (Griewank & Walther, 2008) and its implementations are widely available as open-source modules (Carpenter et al., 2015).

In our framework, the discrete parameters are first embedded into a continuous space, inducing parameters with piecewise constant densities. A key theoretical insight is that Hamiltonian dynamics with a discontinuous potential energy can be integrated analytically near its discontinuity in a way that exactly preserves the total energy. This fact was realized by Pakman & Paninski (2013) and used to sample from binary distributions through embedding them into a continuous space. This framework was slightly extended by Afshar & Domke (2015) to handle more general discontinuous distributions and further adapted by Dinh et al. (2017) to settings where the parameter space involves phylogenetic trees. All these frameworks, however, run into serious computational issues when dealing with more complex discontinuities and thus fail as general-purpose algorithms.

We introduce several novel techniques to obtain a practical sampling algorithm for discrete parameters and, more generally, target distributions with discontinuous densities. We propose a product Laplace distribution for the momentum variable as a more effective alternative to the usual Gaussian distribution in dealing with discontinuous targets. We develop an efficient integrator of Hamiltonian dynamics based on a Laplace momentum by splitting the differential operator into its coordinate-wise components. This integrator exactly preserves the Hamiltonian and leads to a type of *rejection-free* Markovian transitions (Peters & de With, 2012). When applying only one step of the proposed integrator, discontinuous Hamiltonian Monte Carlo coincides with a Metropolis-within-Gibbs sampler. Hence, properly-tuned discontinuous Hamiltonian Monte Carlo is guaranteed to outperform Metropolis-within-Gibbs.

2. HAMILTONIAN MONTE CARLO FOR DISCRETE AND DISCONTINUOUS DISTRIBUTIONS

2.1. Review of Hamiltonian Monte Carlo

Given a parameter $\boldsymbol{\theta} \sim \pi_{\Theta}(\cdot)$ of interest, Hamiltonian Monte Carlo introduces an auxiliary *momentum* variable \mathbf{p} and samples from a joint distribution $\pi(\boldsymbol{\theta}, \mathbf{p}) = \pi_{\Theta}(\boldsymbol{\theta})\pi_P(\mathbf{p})$ for some symmetric distribution $\pi_P(\mathbf{p}) \propto \exp\{-K(\mathbf{p})\}$. The function $K(\mathbf{p})$ is referred to as the *kinetic energy* and $U(\boldsymbol{\theta}) = -\log \pi_{\Theta}(\boldsymbol{\theta})$ as the *potential energy*. The total energy $H(\boldsymbol{\theta}, \mathbf{p}) = U(\boldsymbol{\theta}) + K(\mathbf{p})$ is often called the *Hamiltonian*. A proposal is generated by simulating trajectories of *Hamiltonian dynamics* where the evolution of the state $(\boldsymbol{\theta}, \mathbf{p})$ is governed by *Hamilton's*

equations:

$$\frac{d\boldsymbol{\theta}}{dt} = \nabla_{\mathbf{p}}K(\mathbf{p}), \quad \frac{d\mathbf{p}}{dt} = -\nabla_{\boldsymbol{\theta}}U(\boldsymbol{\theta}) = \nabla_{\boldsymbol{\theta}} \log \pi_{\Theta}(\boldsymbol{\theta}). \quad (1)$$

The next section shows how we can turn the problem of dealing with a discrete parameter $\boldsymbol{\theta}$ to that of dealing with a discontinuous target density. We then proceed to make sense of the differential equation (1) when $\pi_{\Theta}(\boldsymbol{\theta})$, and hence $U(\boldsymbol{\theta})$, is discontinuous.

2.2. Dealing with discrete parameters via embedding: turning it into discontinuous problems

Let N denote a discrete parameter with prior distribution $\pi_N(\cdot)$ and assume without loss of generality that N takes positive integer values $\{1, 2, 3, \dots\}$. For example, the inference goal may be estimation of the population size N given the observation $y | q, N \sim \text{Binomial}(q, N)$ and the prior $N \sim \pi_N(\cdot)$. We embed N into a continuous space by introducing a latent parameter \tilde{N} whose relationship with N is defined to be

$$N = n \quad \text{if and only if} \quad \tilde{N} \in (a_n, a_{n+1}], \quad (2)$$

for an increasing sequence of real numbers $0 = a_1 \leq a_2 \leq a_3 \leq \dots$. To match the prior distribution on N , we define the corresponding prior density on \tilde{N} as

$$\pi_{\tilde{N}}(\tilde{n}) = \sum_{n \geq 1} \frac{\pi_N(n)}{a_{n+1} - a_n} \mathbb{1}\{a_n < \tilde{n} \leq a_{n+1}\}, \quad (3)$$

where the Jacobian-like factor $(a_{n+1} - a_n)^{-1}$ adjusts for embedding into non-uniform intervals.

Although the choice $a_n = n$ for all n is a natural one, a non-uniform embedding is useful in effectively carrying out a parameter transformation of N . For example, a log-transform $a_n = \log n$ may be used to avoid a heavy-tailed distribution on \tilde{N} or to reduce correlation between \tilde{N} and the rest of the parameters. Mixing of many Markov chain Monte Carlo algorithms, including discontinuous Hamiltonian Monte Carlo, can be substantially improved by such parameter transformations (Roberts & Rosenthal, 2009; Thawornwattana et al., 2018).

2.3. How Hamiltonian Monte Carlo fails on discontinuous target densities

Having recast the discrete parameter problem as a discontinuous one, we focus the rest of our discussion on discontinuous targets. An *integrator* is an algorithm that numerically approximates an evolution of the exact solution to a differential equation. Hamiltonian Monte Carlo requires *reversible* and *volume-preserving* integrators to guarantee symmetry of its proposal distributions (see Section 4.1 and Neal, 2010). These proposals are generated as follows:

1. Sample the momentum from its marginal distribution $\mathbf{p} \sim \pi_P(\cdot)$.
2. Using a reversible and volume-preserving integrator, approximate $\{\boldsymbol{\theta}(t), \mathbf{p}(t)\}_{t \geq 0}$, the solution of the differential equation (1) with the initial condition $\{\boldsymbol{\theta}(0), \mathbf{p}(0)\} = (\boldsymbol{\theta}, \mathbf{p})$. Use the approximate solution $(\boldsymbol{\theta}^*, \mathbf{p}^*) \approx \{\boldsymbol{\theta}(\tau), \mathbf{p}(\tau)\}$ for some $\tau > 0$ as a proposal.

The proposal $(\boldsymbol{\theta}^*, \mathbf{p}^*)$ then is accepted with Metropolis probability (Metropolis et al., 1953)

$$\min[1, \exp\{-H(\boldsymbol{\theta}^*, \mathbf{p}^*) + H(\boldsymbol{\theta}, \mathbf{p})\}], \quad (4)$$

where $H(\boldsymbol{\theta}, \mathbf{p}) = -\log \pi(\boldsymbol{\theta}, \mathbf{p})$ denotes the Hamiltonian. With an accurate integrator, the acceptance probability of $(\boldsymbol{\theta}^*, \mathbf{p}^*)$ can be close to 1 because of the *conservation of energy property* of Hamiltonian dynamics: $H\{\boldsymbol{\theta}(t), \mathbf{p}(t)\} = H\{\boldsymbol{\theta}(0), \mathbf{p}(0)\}$ for all $t \geq 0$ for the exact solution. The integrator of choice for Hamiltonian Monte Carlo is the *leapfrog* scheme, which approximates

the evolution $\{\boldsymbol{\theta}(t), \mathbf{p}(t)\} \rightarrow \{\boldsymbol{\theta}(t + \epsilon), \mathbf{p}(t + \epsilon)\}$ by the successive updates

$$\mathbf{p} \leftarrow \mathbf{p} - \frac{\epsilon}{2} \nabla_{\boldsymbol{\theta}} U(\boldsymbol{\theta}), \quad \boldsymbol{\theta} \leftarrow \boldsymbol{\theta} + \epsilon \nabla_{\mathbf{p}} K(\mathbf{p}), \quad \mathbf{p} \leftarrow \mathbf{p} - \frac{\epsilon}{2} \nabla_{\boldsymbol{\theta}} U(\boldsymbol{\theta}). \quad (5)$$

When $\pi_{\Theta}(\cdot)$ is smooth, approximating the evolution $\{\boldsymbol{\theta}(0), \mathbf{p}(0)\} \rightarrow \{\boldsymbol{\theta}(\tau), \mathbf{p}(\tau)\}$ with $L = \lfloor \tau/\epsilon \rfloor$ leapfrog steps results in an error of order $O(\epsilon^2)$ so that $H(\boldsymbol{\theta}^*, \mathbf{p}^*) = H(\boldsymbol{\theta}, \mathbf{p}) + O(\epsilon^2)$. Hamiltonian Monte Carlo's high acceptance rates and scaling properties critically depend on this second-order accuracy of the leapfrog integrator; see discussions in Section 4.4. When $\pi_{\Theta}(\cdot)$ has a discontinuity, however, the leapfrog updates (5) fail to account for the instantaneous change in $\pi_{\Theta}(\cdot)$, incurring unbounded errors that do not decrease even as $\epsilon \rightarrow 0$.

2.4. Theory of discontinuous Hamiltonian dynamics

While a discontinuous function does not have a derivative in a classical sense, the gradient $\nabla U(\boldsymbol{\theta})$ can be defined through a notion of *distributional derivatives* and the corresponding Hamilton's equations (1) can be interpreted as a *measure-valued differential inclusion* (Stewart, 2000). In this case, a solution is in general not unique unlike that of a smooth ordinary differential equation. To find a solution that preserves critical properties of Hamiltonian dynamics, we rely on a so-called *selection principle* (Ambrosio, 2008) as follows.

Define a sequence of smooth approximations $U_{\delta}(\boldsymbol{\theta})$ of $U(\boldsymbol{\theta})$ for $\delta > 0$ through the convolution $U_{\delta} = U * \phi_{\delta}$ with $\phi_{\delta}(\boldsymbol{\theta}) = \delta^{-d} \phi(\delta^{-1}\boldsymbol{\theta})$ for a compactly supported smooth function $\phi \geq 0$ such that $\int \phi = 1$. Here the integer d denotes the dimension of $\boldsymbol{\theta}$. Now let $\{\boldsymbol{\theta}_{\delta}(t), \mathbf{p}_{\delta}(t)\}$ be the solution of Hamilton's equations with the potential energy U_{δ} . It can be shown that the pointwise limit $\{\boldsymbol{\theta}(t), \mathbf{p}(t)\} = \lim_{\delta \rightarrow 0} \{\boldsymbol{\theta}_{\delta}(t), \mathbf{p}_{\delta}(t)\}$ exists for almost every initial condition and we define the dynamics corresponding to $U(\boldsymbol{\theta})$ as this limit. This construction provides a rigorous mathematical foundation for the special cases of discontinuous Hamiltonian dynamics derived by Pakman & Paninski (2013) and Afshar & Domke (2015) through physical heuristics.

The behavior of the limiting dynamics near the discontinuity is deduced as follows. Suppose that the trajectory $\{\boldsymbol{\theta}(t), \mathbf{p}(t)\}$ hits the discontinuity at an event time t_e and let t_e^- and t_e^+ denote infinitesimal moments before and after that. Since the discontinuity set of $U(\boldsymbol{\theta})$ was assumed to be piecewise smooth, at a discontinuity point $\boldsymbol{\theta}$ we have

$$\lim_{\delta \rightarrow 0} \nabla_{\boldsymbol{\theta}} U_{\delta}(\boldsymbol{\theta}) / \|\nabla_{\boldsymbol{\theta}} U_{\delta}(\boldsymbol{\theta})\| = \boldsymbol{\nu}(\boldsymbol{\theta}), \quad (6)$$

where $\boldsymbol{\nu}(\boldsymbol{\theta})$ denotes a unit vector orthonormal to the discontinuity boundary, pointing in the direction of higher potential energy. Here we assume that $U(\boldsymbol{\theta})$ is piecewise smooth, so that such an orthonormal vector is well-defined except on a set of measure zero. The relations (6) and $d\mathbf{p}_{\delta}/dt = -\nabla_{\boldsymbol{\theta}} U_{\delta}$ imply that the only change in $\mathbf{p}(t)$ upon encountering the discontinuity occurs in the direction of $\boldsymbol{\nu}_e = \boldsymbol{\nu}\{\boldsymbol{\theta}(t_e)\}$:

$$\mathbf{p}(t_e^+) = \mathbf{p}(t_e^-) - \gamma \boldsymbol{\nu}_e \quad (7)$$

for some $\gamma > 0$. There are two possible types of change in \mathbf{p} depending on the potential energy difference ΔU_e at the discontinuity, which we formally define as

$$\Delta U_e = \lim_{\epsilon \rightarrow 0^+} U\{\boldsymbol{\theta}(t_e) + \epsilon \mathbf{p}(t_e^-)\} - U\{\boldsymbol{\theta}(t_e^-)\}. \quad (8)$$

When the momentum does not provide enough kinetic energy to overcome the potential energy increase ΔU_e , the trajectory bounces against the plane orthogonal to $\boldsymbol{\nu}_e$. Otherwise, the trajectory moves through the discontinuity by transferring kinetic energy to potential energy. Either way, the magnitude of an instantaneous change γ can be determined via the energy conservation law:

$$K\{\mathbf{p}(t_e^+)\} - K\{\mathbf{p}(t_e^-)\} = U\{\boldsymbol{\theta}(t_e^-)\} - U\{\boldsymbol{\theta}(t_e^+)\}. \quad (9)$$

Figure 1, which is explained in more details in Section 3, provides a visual illustration of the trajectory behavior at a discontinuity.

3. INTEGRATOR FOR DISCONTINUOUS DYNAMICS VIA LAPLACE MOMENTUM

3.1. Limitation of Gaussian momentum-based approaches

Use of non-Gaussian momentums has received limited attention in the Hamiltonian Monte Carlo literature. Correspondingly, the existing discontinuous extensions all rely on Gaussian momentums (Pakman & Paninski, 2013; Afshar & Domke, 2015; Dinh et al., 2017).

In developing a general-purpose algorithm for sampling from discontinuous targets, however, dynamics based on a Gaussian momentum have a serious shortcoming. In order to approximate the dynamics accurately, the integrator must detect every single discontinuity encountered by a trajectory and then compute the potential energy difference each time (see supplement Section A). To see why this is a serious problem, consider a discrete parameter $N \in \mathbb{Z}^+$ with a substantial posterior uncertainty, say $\text{Var}(N \mid \text{data})^{1/2} \approx 1000$. We can then expect a Metropolis move like $N \rightarrow N \pm 1000$ to be accepted with a moderate probability, costing only a single likelihood evaluation. On the other hand, if we were to sample a continuously embedded counter part \tilde{N} of N using discontinuous Hamiltonian Monte Carlo with the Gaussian momentum-based integrator of Algorithm S1, a transition of the corresponding magnitude necessarily requires *1000 likelihood evaluations*. The algorithm is made practically useless by such a high computational cost for otherwise simple parameter updates.

3.2. Hamiltonian dynamics based on Laplace momentum

The above example exposes a major challenge in turning discontinuous Hamiltonian dynamics into a practical general-purpose sampling algorithm for discontinuous targets: we need an integrator that can jump through multiple discontinuities in a small number of target density evaluations while approximately preserving the total energy. We provide a solution by employing a product Laplace distribution $\pi_P(\mathbf{p}) \propto \prod_i \exp(-m_i^{-1}|p_i|)$. While similar momentum distributions have been considered for improving numerical stability and mixing rate within the traditional Hamiltonian Monte Carlo framework (Zhang et al., 2016; Lu et al., 2016; Livingstone et al., 2016), we exploit a unique feature of the Laplace momentum in a fundamentally new way.

Hamilton’s equation under the independent Laplace momentum is given by

$$\frac{d\boldsymbol{\theta}}{dt} = \mathbf{m}^{-1} \odot \text{sign}(\mathbf{p}), \quad \frac{d\mathbf{p}}{dt} = -\nabla_{\boldsymbol{\theta}} U(\boldsymbol{\theta}), \quad (10)$$

where \odot denotes element-wise multiplication. A unique characteristic of the dynamics (10) is that the time derivative of $\boldsymbol{\theta}(t)$ depends only on the signs of p_i ’s and not on their magnitudes. In particular, if we know that $p_i(t)$ ’s do not change their signs on the time interval $t \in [\tau, \tau + \epsilon]$, then we also know that

$$\boldsymbol{\theta}(\tau + \epsilon) = \boldsymbol{\theta}(\tau) + \epsilon \mathbf{m}^{-1} \odot \text{sign}\{\mathbf{p}(\tau)\} \quad (11)$$

irrespective of the intermediate values $U\{\boldsymbol{\theta}(t)\}$ along the trajectory $\{\boldsymbol{\theta}(t), \mathbf{p}(t)\}$ for $t \in [\tau, \tau + \epsilon]$. Our integrator’s ability to jump through multiple discontinuities of $U(\boldsymbol{\theta})$ in a single target density evaluation depends critically on this property of the dynamics.

3.3. Integrator for Laplace momentum via operator splitting

Operator splitting is a technique to approximate the solution of a differential equation by decomposing it into components, each of which can be solved more easily (McLachlan & Quispel,

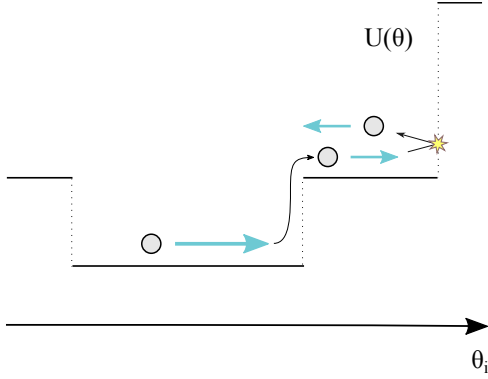


Fig. 1. An example trajectory $\theta(t)$ of discontinuous Hamiltonian dynamics. The trajectory has enough kinetic energy to move across the first discontinuity by transferring some kinetic energy to potential energy. Across the second discontinuity, however, the trajectory has insufficient kinetic energy to compensate for the potential energy increase and bounces back as a result.

2002). More commonly used Hamiltonian splitting methods are special cases (Neal, 2010). A convenient splitting scheme for (10) can be devised by considering the equation for each coordinate (θ_i, p_i) while keeping the other parameters (θ_{-i}, p_{-i}) fixed:

$$\frac{d\theta_i}{dt} = m_i^{-1} \text{sign}(p_i), \quad \frac{dp_i}{dt} = -\partial_{\theta_i} U(\theta), \quad \frac{d\theta_{-i}}{dt} = \frac{dp_{-i}}{dt} = \mathbf{0}. \quad (12)$$

There are two possible behaviors for the solution $\{\theta(t), p(t)\}$ of (12) for $t \in [\tau, \tau + \epsilon]$, depending on the initial momentum $p_i(\tau)$. Let $\theta^*(t)$ denote a potential path of $\theta(t)$:

$$\theta_i^*(t) = \theta_i(\tau) + (t - \tau)m_i^{-1} \text{sign}(p_i(\tau)), \quad \theta_{-i}^*(t) = \theta_{-i}(\tau). \quad (13)$$

In case the initial momentum is large enough that $m_i^{-1}|p_i(\tau)| > U\{\theta^*(t)\} - U\{\theta(\tau)\}$ for all $t \in [\tau, \tau + \epsilon]$, we have

$$\theta(\tau + \epsilon) = \theta^*(\tau + \epsilon) = \theta(\tau) + \epsilon m_i^{-1} \text{sign}\{p_i(\tau)\} e_i \quad (14)$$

Otherwise, the momentum p_i flips ($p_i \leftarrow -p_i$) and the trajectory $\theta(t)$ reverses its course at the event time t_e given by

$$t_e = \inf \left\{ t \in [\tau, \tau + \epsilon] : U\{\theta^*(t)\} - U\{\theta(\tau)\} > K\{p(\tau)\} \right\}. \quad (15)$$

See Figure 1 for a visual illustration of the trajectory $\theta(t)$.

By emulating the behavior of the solution $\{\theta(t), p(t)\}$, we obtain an efficient integrator of the coordinate-wise equation (12) as given in Algorithm 1. While the parameter θ does not get updated when $m_i^{-1}|p_i| < \Delta U$ (line 5), the momentum flip $p_i \leftarrow -p_i$ (line 9) ensures that the next numerical integration step leads the trajectory toward a higher density of $\pi_{\Theta}(\theta)$.

The solution of the original (unsplit) differential equation (10) is approximated by sequentially updating each coordinate of (θ, p) with Algorithm 1 as illustrated in Figure 2. The reversibility of the resulting proposal is guaranteed by randomly permuting the order of the coordinate updates. Alternatively, one can split the operator symmetrically to obtain a reversible integrator (McLachlan & Quispel, 2002). The integrator does not reproduce the exact solution but nonetheless preserves the Hamiltonian exactly, yielding a rejection-free proposal. While this remains true with any stepsize ϵ , for good mixing the stepsize needs to be chosen small enough that the condition on Line 5 is satisfied with high probability (Section S3).

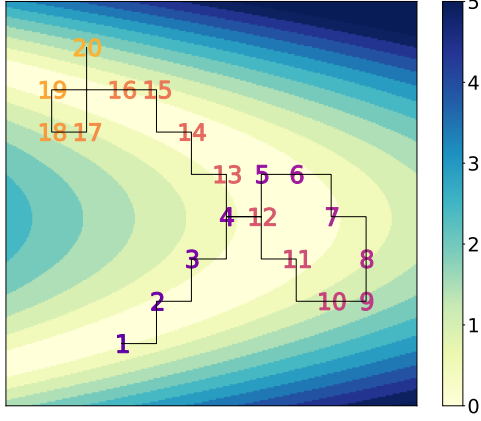


Fig. 2. A trajectory of Laplace momentum based Hamiltonian dynamics $\{\theta_1(t), \theta_2(t)\}$ approximated by the coordinate-wise integrator of Algorithm 1. The log density of the target distribution changes in the increment of 0.5 and has “banana-shaped” contours. Each numerical integration step consists of the coordinate-wise update along the horizontal axis followed by that along the vertical axis. The order of the coordinate updates is randomized at the beginning of numerical integration to ensure reversibility. The trajectory initially travels in the direction of the initial momentum, a process marked by the numbers 1–4. At the 5th numerical integration step, however, the trajectory does not have sufficient kinetic energy to take a step upward and hence flips the momentum downward. Such momentum flips also occur at the 8th and 9th numerical integration steps, again changing the direction of the trajectory. The rest of the trajectory follows the same pattern.

Algorithm 1. Coordinate-wise integrator for dynamics with Laplace momentum

1 Function

CoordIntegrator ($\theta, \mathbf{p}, i, \epsilon$):

```

2    $\theta^* \leftarrow \theta$ 
3    $\theta_i^* \leftarrow \theta_i^* + \epsilon m_i^{-1} \text{sign}(p_i)$ 
4    $\Delta U \leftarrow U(\theta^*) - U(\theta)$ 
5   if  $m_i^{-1} |p_i| > \Delta U$  then
6      $\theta_i \leftarrow \theta_i^*$ 
7      $p_i \leftarrow p_i - \text{sign}(p_i) m_i \Delta U$ 
8   else
9      $p_i \leftarrow -p_i$ 
10  return  $\theta, \mathbf{p}$ 

```

Algorithm 2. Integrator for discontinuous Hamiltonian Monte Carlo

Function

DiscIntegrator ($\theta, \mathbf{p}, \epsilon, \varphi = \text{Permute}(J)$):

```

 $\mathbf{p}_I \leftarrow \mathbf{p}_I + \frac{\epsilon}{2} \nabla_{\theta_I} \log \pi(\theta)$ 
 $\theta_I \leftarrow \theta_I + \frac{\epsilon}{2} M_I^{-1} \mathbf{p}_I$ 
for  $j$  in  $J$  do
   $\theta, \mathbf{p} \leftarrow \text{CoordIntegrator}(\theta, \mathbf{p}, \varphi(j), \epsilon)$ 
  // Update discontinuous params
 $\theta_I \leftarrow \theta_I + \frac{\epsilon}{2} M_I^{-1} \mathbf{p}_I$ 
 $\mathbf{p}_I \leftarrow \mathbf{p}_I + \frac{\epsilon}{2} \nabla_{\theta_I} \log \pi(\theta)$ 
return  $\theta, \mathbf{p}$ 

```

3.4. Mixing momentum distributions for continuous and discrete parameters

The potential energy $U(\theta)$ is a smooth function of θ_i if both the prior and likelihood depend smoothly on θ_i . The coordinate-wise update of Algorithm 1 leads to a valid proposal mechanism whether or not $U(\theta)$ has discontinuities along the coordinate θ_i . If $U(\theta)$ varies smoothly along some coordinates of θ , however, we can devise an integrator that takes advantage of such smooth dependence.

We first write $\theta = (\theta_I, \theta_J)$ where the collections of indices I and J are defined as

$$I = \{i \in \{1, \dots, d\} : U(\theta) \text{ is a smooth function of } \theta_i\}, \quad J = \{1, \dots, d\} \setminus I. \quad (16)$$

More precisely, we assume that the parameter space has a partition $\mathbb{R}^{|I|} \times \mathbb{R}^{|J|} = \cup_k \mathbb{R}^{|I|} \times \Omega_k$ such that $U(\theta)$ is smooth on $\mathbb{R}^{|I|} \times \Omega_k$ for each k . We write $\mathbf{p} = (\mathbf{p}_I, \mathbf{p}_J)$ correspondingly and define the distribution of \mathbf{p} as a product of Gaussian and Laplace so that

$$K(\mathbf{p}) = -\log \pi_P(\mathbf{p}) = \frac{1}{2} \mathbf{p}_I^\top M_I^{-1} \mathbf{p}_I + \sum_{j \in J} m_j^{-1} |p_j|, \quad (17)$$

where M_I and $M_J = \text{diag}(\mathbf{m}_J)$ are mass matrices (Neal, 2010). With slight abuse of terminology, we will refer to (θ_J, \mathbf{p}_J) as discontinuous parameters.

When mixing Gaussian and Laplace momentums, we approximate the dynamics via an integrator based again on operator splitting; we update the smooth parameter $(\boldsymbol{\theta}_I, \mathbf{p}_I)$ first, then the discontinuous parameter $(\boldsymbol{\theta}_J, \mathbf{p}_J)$, followed by another update of $(\boldsymbol{\theta}_I, \mathbf{p}_I)$. The discontinuous parameters are updated coordinate-wise as described in Section 3.3. The update of $(\boldsymbol{\theta}_I, \mathbf{p}_I)$ is based on a decomposition familiar from the leapfrog scheme:

$$\frac{d\mathbf{p}_I}{dt} = \nabla_{\boldsymbol{\theta}_I} \log \pi(\boldsymbol{\theta}), \quad \frac{d\boldsymbol{\theta}_I}{dt} = \mathbf{0}, \quad \frac{d\boldsymbol{\theta}_J}{dt} = \frac{d\mathbf{p}_J}{dt} = \mathbf{0}, \quad (18)$$

$$\frac{d\boldsymbol{\theta}_I}{dt} = \mathbf{M}_I^{-1} \mathbf{p}_I, \quad \frac{d\mathbf{p}_I}{dt} = \mathbf{0}, \quad \frac{d\boldsymbol{\theta}_J}{dt} = \frac{d\mathbf{p}_J}{dt} = \mathbf{0}. \quad (19)$$

The pseudo code of Algorithm 2 describes the integrator with all the ingredients put together. When mixing in Gaussian momentums, the integrator continues to preserve the Hamiltonian very accurately if not exactly (supplement Section S8). Despite the proposal being not necessarily rejection-free in this case, advantages of treating continuous and discontinuous parameters separately are discussed in supplement Section S2.

4. THEORETICAL PROPERTIES OF DISCONTINUOUS HAMILTONIAN MONTE CARLO

4.1. Reversibility of discontinuous Hamiltonian Monte Carlo transition kernel

As for existing Hamiltonian Monte Carlo variants, the reversibility of discontinuous Hamiltonian Monte Carlo is a direct consequence of the reversibility and volume-preserving property of our integrator in Algorithm 2 (Neal, 2010; Fang et al., 2014). We thus focus on establishing these properties of our integrator. Let Ψ denote a bijective map on the space $(\boldsymbol{\theta}, \mathbf{p})$ corresponding to the approximation of discontinuous Hamiltonian dynamics through multiple numerical integration steps. An integrator is *reversible* if Ψ satisfies

$$(\mathbf{R} \circ \Psi)^{-1} = \mathbf{R} \circ \Psi \quad \text{or equivalently} \quad \Psi^{-1} = \mathbf{R} \circ \Psi \circ \mathbf{R} \quad (20)$$

where $\mathbf{R} : (\boldsymbol{\theta}, \mathbf{p}) \rightarrow (\boldsymbol{\theta}, -\mathbf{p})$ is a momentum flip operator. Due to the updates of discrete parameters in a random order, the map Ψ induced by our integrator is non-deterministic. Consequently, our integrator has an unconventional feature of being reversible “in distribution” only, $(\mathbf{R} \circ \Psi)^{-1} \stackrel{d}{=} \mathbf{R} \circ \Psi$, which is sufficient for the resulting Markov chain to be reversible.

LEMMA 1. *For a piecewise smooth potential energy $U(\boldsymbol{\theta})$, the coordinate-wise integrator of Algorithm 1 is volume-preserving and reversible for any coordinate index i except on a set of measure zero. Moreover, updating multiple coordinates with the integrator in a random order $\varphi(1), \dots, \varphi(d)$ is again reversible in distribution provided that the random permutation φ satisfies $\{\varphi(1), \varphi(2), \dots, \varphi(d)\} \stackrel{d}{=} \{\varphi(d), \varphi(d-1), \dots, \varphi(1)\}$.*

THEOREM 1. *For a piecewise smooth potential energy $U(\boldsymbol{\theta})$, the integrator of Algorithm 2 is volume-preserving and reversible except on a set of measure zero.*

The proofs are in Appendix A.

We also establish in Theorem 2 below the reversibility and volume-preserving property of discontinuous Hamiltonian dynamics with alternative kinetic energies. Theorem 2 extends the result of Afshar & Domke (2015) and justifies the use of the Gaussian momentum-based integrator Algorithm S1 in the supplement. A *solution operator* Ψ_t of a differential equation, or more generally of a differential inclusion, is a map such that $\{\boldsymbol{\theta}(t), \mathbf{p}(t)\} = \Psi_t(\boldsymbol{\theta}_0, \mathbf{p}_0)$ is a solution of the equation with the initial condition $\{\boldsymbol{\theta}(0), \mathbf{p}(0)\} = (\boldsymbol{\theta}_0, \mathbf{p}_0)$. Also, *symplecticity* is a property of Hamiltonian dynamics which implies volume-preservation. Supplement Section S7 provides the definition of symplecticity as well as the proof of Theorem 2.

THEOREM 2. *Let $U(\boldsymbol{\theta})$ be a piecewise constant potential energy function whose discontinuity set is piecewise linear. Suppose that a kinetic energy $K(\mathbf{p})$ is symmetric, convex, piecewise smooth, and satisfies the growth condition $K(\mathbf{p}) \rightarrow \infty$ as $\|\mathbf{p}\| \rightarrow \infty$. Then the solution operator Ψ_t of discontinuous Hamiltonian dynamics as defined in Section 2.4 is symplectic and reversible except on a set of measure zero.*

4.2. Irreducibility via randomized stepsize

Irreducibility and aperiodicity hold trivially for most chains, but care needs to be taken when applying the coordinate-wise integrator for discontinuous Hamiltonian Monte Carlo; its use with a fixed stepsize ϵ results in a reducible Markov chain which is not ergodic. To see the issue, consider the transition probability of multiple iterations of discontinuous Hamiltonian Monte Carlo based on the integrator of Algorithm 2. Given the initial state $\boldsymbol{\theta}_0$, the integrator of Algorithm 1 moves the i -th coordinate of $\boldsymbol{\theta}$ only by the distance $\pm \epsilon m_i^{-1}$ regardless of the values of the momentum variable. The transition probability in the $\boldsymbol{\theta}$ -space with \mathbf{p} marginalized out, therefore, is supported on a grid

$$\Omega = \{(\boldsymbol{\theta}_I, \boldsymbol{\theta}_J) : \boldsymbol{\theta}_J = \boldsymbol{\theta}_{0,J} + \epsilon \mathbf{m} \odot \mathbf{k} \text{ for a vector of integers } \mathbf{k}\}, \quad (21)$$

where $\boldsymbol{\theta}_J$ as in (16) denotes the coordinates of $\boldsymbol{\theta}$ with discontinuous conditionals.

This pathological behavior can be avoided by randomizing the stepsize at each iteration, say $\epsilon \sim \text{Unif}(\epsilon_{\min}, \epsilon_{\max})$. Randomizing the stepsize additionally addresses a possibility that some regions of the parameter space requires smaller stepsizes for efficient exploration (Neal, 2010). While the coordinate-wise integrator does not suffer from the stability issue of the leapfrog scheme, the quantity ϵm_i^{-1} nonetheless needs to be in the same order of magnitude as the length scale of θ_i ; see supplement Section S3.

4.3. Metropolis-within-Gibbs with momentum as special case

Consider a version of discontinuous Hamiltonian Monte Carlo in which all the parameters are updated with the coordinate-wise integrator of Algorithm 1; in other words, the integrator of Algorithm 2 is applied with $J = \{1, \dots, d\}$ and an empty indexing set I . This version is a generalization of random-scan Metropolis-within-Gibbs, also known as one-variable-at-a-time Metropolis. We therefore refer to this version as *Metropolis-within-Gibbs with momentum*.

We use $\pi_\epsilon(\cdot)$ and $\pi_\Phi(\cdot)$ to denote the distribution of a stepsize ϵ and a permutation φ of $\{1, \dots, d\}$. The distribution $\pi_\Phi(\cdot)$ is required to satisfy $\{\varphi(1), \dots, \varphi(d)\} \stackrel{d}{=} \{\varphi(d), \dots, \varphi(1)\}$. With these notations, each iteration of Metropolis-within-Gibbs with momentum can be expressed as follows:

1. Draw $\epsilon \sim \pi_\epsilon(\cdot)$, $\varphi \sim \pi_\Phi(\cdot)$, and $p_j \sim \text{Laplace}(\text{scale} = m_j)$ for $j = 1, \dots, d$.
2. Repeat for L times a sequential update of the coordinate (θ_j, p_j) for $j = \varphi(1), \dots, \varphi(d)$ via Algorithm 1 with stepsize ϵ .

In this version of discontinuous Hamiltonian Monte Carlo, the integrator exactly preserves the Hamiltonian and the acceptance-rejection step can be omitted.

When $L = 1$, the above algorithm recovers random-scan Metropolis-within-Gibbs. This can be seen by realizing that Lines 5 – 9 of Algorithm 1 coincide with the standard Metropolis acceptance-rejection procedure for θ_j . More precisely, the coordinate-wise integrator updates θ_j to $\theta_j + \epsilon m_j^{-1} \text{sign}(p_j)$ only if

$$\exp\{-U(\boldsymbol{\theta}^*) + U(\boldsymbol{\theta})\} > \exp(-m_j^{-1}|p_j|) \stackrel{d}{=} \text{Unif}(0, 1), \quad (22)$$

where the last distributional equality follows from the fact $m_j^{-1}|p_j| \stackrel{d}{=} \text{Exp}(1)$. To summarize, when taking only one numerical integration step, the version of discontinuous Hamiltonian Monte Carlo considered here coincides with Metropolis-within-Gibbs with a random scan order $\varphi \sim \pi_\Phi(\cdot)$ and a symmetric proposal $\theta_j \pm \epsilon m_j^{-1}$ for each parameter with $\epsilon \sim \pi_\mathcal{E}(\cdot)$. This formulation of Metropolis-within-Gibbs has the univariate proposal distributions coupled via the shared parameter $\epsilon \sim \pi_\mathcal{E}(\cdot)$. We could also consider a version of discontinuous Hamiltonian Monte Carlo with a fixed stepsize $\epsilon = 1$ but with a mass matrix randomized $(m_1^{-1}, \dots, m_d^{-1}) \sim \pi_{M^{-1}}(\cdot)$ before each numerical integration step. This version would correspond to a more standard Metropolis-within-Gibbs with independent univariate proposals.

Being a generalization of Metropolis-within-Gibbs, discontinuous Hamiltonian Monte Carlo is guaranteed a superior performance:

COROLLARY 1. *Under any efficiency metric, which may account for computational costs per iteration, an optimally tuned discontinuous Hamiltonian Monte Carlo is guaranteed to outperform a class of random-scan Metropolis-within-Gibbs samplers as described above.*

In particular, an optimally tuned discontinuous Hamiltonian Monte Carlo will inherit the geometric ergodicity of a corresponding Metropolis-within-Gibbs sampler, sufficient conditions for which are investigated in Johnson et al. (2013). In practice, the addition of momentum to Metropolis-within-Gibbs allows for a more efficient update of correlated parameters as empirically confirmed in the supplement Section S6.1.

4.4. Scalability in the number of parameters

Beskos et al. (2013) analyzes the scaling of the computational cost of Hamiltonian Monte Carlo as the number of parameters d grows. For a target distribution of the form $\pi(\boldsymbol{\theta}) = \prod_{i=1}^d \pi_0(\theta_i)$, they show that the cost needs to scale as $O(d^{5/4})$ to maintain a $O(1)$ acceptance probability. This scaling property is superior to those of Metropolis-adjusted Langevin and random-walk Metropolis algorithms and, in essence, a consequence of the fact that the global error in Hamiltonian incurred by the leapfrog integrator is $O(\epsilon^2)$. As we show in the supplement Section S8, the global error in Hamiltonian by the discontinuous Hamiltonian Monte Carlo integrator of Algorithm 2 is also $O(\epsilon^2)$. It can therefore be expected that the scaling property of discontinuous Hamiltonian Monte Carlo is comparable to that of Hamiltonian Monte Carlo.

Since the coordinate-wise integrator of Algorithm 1 incurs no error in Hamiltonian, the version described in Section 4.3 potentially has a superior scaling property depending on the structure of the target distribution. For example, if a sequential evaluation of all the individual conditional distributions can be carried out with $O(d)$ computation, then the version could have $O(d)$ scaling.

5. NUMERICAL RESULTS

5.1. Experimental set-up, benchmarks, and efficiency metric

We use two challenging posterior inference problems to demonstrate that discontinuous Hamiltonian Monte Carlo is an efficient general-purpose sampler. Additional numerical results in the supplement Section S6 further illustrate the breadth of its capability. Codes to reproduce the simulation results are available at <https://github.com/aki-nishimura/discontinuous-hmc>.

Few general and efficient approaches currently exist for sampling from a discrete parameter or a discontinuous target density. For each of the numerical results, therefore, we pick a few most appropriate general-purpose samplers to benchmark against. Chopin & Ridgway (2017) compare a variety of algorithms in the context of sampling from posterior distributions in binary classifica-

tion problems. One of their conclusions is that, while random-walk Metropolis is known to scale poorly in the number of parameters (Roberts et al., 1997), Metropolis with a properly adapted proposal covariance is competitive with alternatives even in dimensions as large as 180. We thus use random-walk Metropolis as one of our benchmarks, choosing proposal covariances proportional to estimates of the target covariances (Roberts et al., 1997; Haario et al., 2001). When the conditional densities can be efficiently evaluated and dependence among the parameters is not too strong, Metropolis-within-Gibbs with component-wise adaptation can scale better than joint-sampling via random-walk Metropolis (Haario et al., 2005). Hence, this approach is used as another benchmark.

For models with discrete parameters, as a further benchmark we use a No-U-turn / Gibbs sampler (Salvatier et al., 2016), which updates continuous parameters with the no-U-turn sampler of Hoffman & Gelman (2014). The standard implementation updates discrete parameters with univariate Metropolis, but here we implement full conditional univariate updates via manually-optimized multinomial samplings.

In all our numerical results, continuous parameters with range constraints are transformed into unconstrained ones to facilitate sampling. More precisely, the constraint $\theta > 0$ is handled by a log transform $\theta \rightarrow \log \theta$ and $\theta \in [0, 1]$ by a logit transform $\theta \rightarrow \log \{\theta/(1 - \theta)\}$ as done in Stan and PyMC (Stan Development Team, 2016; Salvatier et al., 2016). For each example, the stepsize and path length for discontinuous Hamiltonian Monte Carlo were manually adjusted over short preliminary runs by visually examining trace plots. The path length here refers to the number of numerical integration steps. The stepsize for the continuous parameter updates of No-U-turn / Gibbs was adjusted analogously.

Efficiencies of the algorithms are compared through effective sample sizes (Geyer, 2011). As is commonly done in the Markov chain Monte Carlo literature, we compute the effective sample sizes of the first and second moment estimators for each parameter and report the minimum value across all the parameters. Effective sample size's are estimated using the method of batch means with 25 batches (Geyer, 2011), averaged over the estimates from 8 independent chains.

5.2. Jolly-Seber model: estimation of unknown open population size and survival rate from multiple capture-recapture data

The Jolly-Seber model and its numerous extensions are widely used in ecology to estimate unknown population sizes as well as related parameters of interest (Schwarz & Seber, 1999). The model is motivated by the following experimental design. Individuals from a particular species are captured, marked, and released back to the environment. This procedure is repeated over multiple capture occasions. At each occasion, the number of marked and unmarked individuals among the captured ones are recorded. Individuals survive from one capture occasion to another with an unknown survival rate. Also, the population is assumed to be “open” so that individuals may enter, either through birth or immigration, or leave the area under study.

In order to be consistent with the literature on capture-recapture models, the notations within this section will deviate from the rest of the paper. Assuming that data are collected over $i = 1, \dots, T$ capture occasions, the unknown parameters of the model are $\{U_i, p_i\}_{i=1}^T$ and $\{\phi_i\}_{i=1}^{T-1}$, each of which represents

U_i = number of unmarked animals right before the i th capture occasion;

p_i = capture probability of each animal at the i th capture occasion;

ϕ_i = survival probability of each animal from the i th to $(i + 1)$ th capture occasion.

Table 1. Performance summary of each algorithm on the Jolly-Serber model example. “DHMC” and “ESS” in the table stand for discontinuous Hamiltonian Monte Carlo and effective sample size. The term $(\pm \dots)$ indicates the error estimate, twice the standard deviations, of our effective sample size estimators. Path length is averaged over each iteration. “Iter time” shows the computational time per iteration of each algorithm relative to the fastest one.

	ESS per 100 samples	ESS per minute	Path length	Iter time
DHMC (diagonal)	45.5 (± 5.2)	424	45	87.7
DHMC (identity)	24.1 (± 2.6)	126	77.5	157
No-U-turn / Gibbs	1.04 (± 0.087)	6.38	150	133
Metropolis	0.0714 (± 0.016)	58.5	1	1

We assign standard objective priors $p_i, \phi_i \sim \text{Unif}(0, 1)$ and $\pi(U_1) \propto U_1^{-1}$. The prior conditional distributions $U_{i+1} | U_i, \phi_i$ require more thought and are described in the supplement Section S5, along with the likelihood function and other details on the Jolly-Seber model.

We take the black-knead capsid population data from Jolly (1965) as summarized in Seber (1982). The data record the capture-recapture information over $T = 13$ successive capture occasions, giving rise to a 38-dimensional posterior distribution involving 13 discrete parameters. We use the log-transformed embedding for the discrete parameter U_i ’s (Section 2.2). No-U-turn / Gibbs sampler updates U_i ’s through multinomial samplings from the integers between 0 and 5,000. The proposal covariance for random-walk Metropolis is chosen by pre-computing the true posterior covariance with a long adaptive Metropolis chain (Haario et al., 2001) and then scaling it according to Roberts et al. (1997). Discontinuous Hamiltonian Monte Carlo can also take advantage of the posterior covariance information, so we also try using a diagonal mass matrix whose entries are set according to the estimated posterior variance of each parameter (supplement Section S3). Starting from stationarity, we run 10^4 iterations of discontinuous Hamiltonian Monte Carlo and No-U-turn / Gibbs and 5×10^5 iterations of Metropolis.

The performance of each algorithm is summarized in Table 1 where “DHMC (diagonal)” and “DHMC (identity)” indicate discontinuous Hamiltonian Monte Carlo with a diagonal and identity mass matrix respectively. The table clearly indicates a superior performance over No-U-turn / Gibbs and Metropolis with approximately 60 and 7-fold efficiency increase respectively when using a diagonal mass matrix. The posterior distribution exhibits high negative correlations between U_i and p_i (Figure 3), being the computational bottleneck for all the algorithms; they all record the worst effective sample size in the first capture probability p_1 .

5.3. Generalized Bayesian belief update based on loss functions

Motivated by model misspecification and difficulty in modeling all aspects of a data generating process, Bissiri et al. (2016) propose a generalized Bayesian framework, which replaces the log-likelihood with a surrogate based on a utility function. Given an additive loss $\ell(y, \theta)$ for the data y and parameter of interest θ , the prior $\pi(\theta)$ is updated to obtain the generalized posterior:

$$\pi_{\text{post}}(\theta) \propto \exp\{-\ell(y, \theta)\} \pi(\theta). \quad (23)$$

While (23) coincides with a pseudo-likelihood type approach, Bissiri et al. (2016) derives the formula as a coherent and optimal update from a decision theoretic perspective.

Here we consider a binary classification problem with an error-rate loss:

$$\ell(\mathbf{y}, \beta) = \sum_{i=1} \mathbb{1}\{y_i \mathbf{x}_i^\top \beta < 0\}, \quad (24)$$

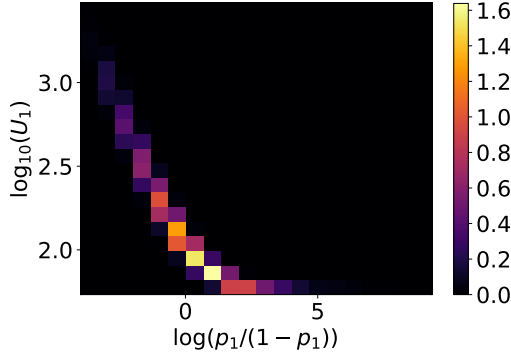


Fig. 3. The posterior marginal of (p_1, U_1) with parameter transformations, estimated from the Monte Carlo samples.

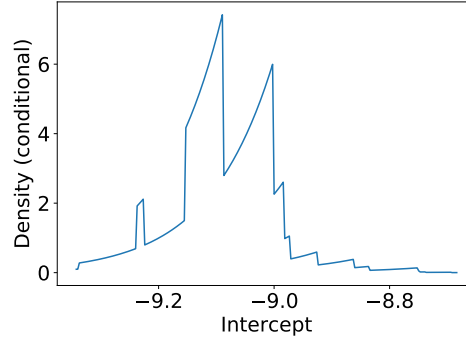


Fig. 4. The posterior conditional density of the intercept parameter in the generalized Bayes example. The other parameters are fixed at the posterior draw that recorded the highest posterior density among the Monte Carlo samples. The density is not continuous since the loss function is not.

where $y_i \in \{-1, 1\}$, x_i is a vector of predictors, and β is a regression coefficient. The target distribution of the form (23) based on the loss function (24) is suggested as a challenging test case by Chopin & Ridgway (2017). We use the SECOM data from the UCI machine learning repository, which records various sensor data that can be used to predict the production quality of a semi-conductor, measured as “pass” or “fail.” We first remove the predictors with more than 20 missing cases and then remove the observations that still had missing predictors, leaving 1,477 cases with 376 predictors. All the predictors are normalized and the regression coefficients β_i ’s are given $\mathcal{N}(0, 1)$ priors. Figure 4 illustrates the complexity of the target distribution.

In tuning the proposal covariance of Metropolis for this example, the performance of adaptive Metropolis proved so poor that we instead use 10^5 iterations of discontinuous Hamiltonian Monte Carlo to estimate the posterior covariance. Scaling the proposal covariance for random-walk Metropolis according to Roberts et al. (1997) resulted in an acceptance probability of less than 4%, so we scaled the proposal covariance to achieve the acceptance probability of 0.234 with stochastic optimization (Andrieu & Thoms, 2008). We also found the posterior correlation to be very modest in this example, with the ratio of the largest and smallest eigenvalues of the estimated posterior covariance matrix being approximately $46 \approx 6.8^2$. This suggests coordinate-wise updates may be competitive, so we implemented Metropolis-within-Gibbs as an additional benchmark. The parameters are updated one at a time with the acceptance probability calibrated around 0.44 as recommended in Gelman et al. (1996). We run discontinuous Hamiltonian Monte Carlo for 10^4 iterations, Metropolis for 10^7 iterations, and Metropolis-within-Gibbs for 5×10^4 iterations from stationarity.

Table 2 summarizes the performance of each algorithm. Discontinuous Hamiltonian Monte Carlo outperforms Metropolis and Metropolis-within-Gibbs approximately by a factor of 330 and 2 respectively. The mixing of Metropolis suffers substantially from the dimensionality of the target (377 parameters). Conditional updates of Metropolis-within-Gibbs mix well in this example due to weak dependence among the parameters. On the other hand, as demonstrated in the example here and in Section 5.2, discontinuous Hamiltonian Monte Carlo not only scales well in the number of parameters but also efficiently handles distributions with strong correlations.

Table 2. Performance summary of each algorithm on the generalized Bayesian posterior example. “DHMC” and “ESS” in the table stand for discontinuous Hamiltonian Monte Carlo and effective sample size. The term $(\pm \dots)$ is the error estimate of our effective sample size estimators. Path length is averaged over each iteration. “Iter time” shows the computational time for one iteration of each algorithm relative to the fastest one.

	ESS per 100 samples	ESS per minute	Path length	Iter time
DHMC	26.3 (± 3.2)	76	25	972
Metropolis	0.00809 (± 0.0018)	0.227	1	1
Metropolis-within-Gibbs	0.514 (± 0.039)	39.8	1	36.2

A. PROOF OF LEMMA 1 AND THEOREM 1

Proof Lemma 1. Assume $p_i \neq 0$ for now and let \mathbf{e}_i denote the i th standard basis vector. Then one step of Algorithm 1 corresponds to a map $\Psi_{i,\epsilon} : (\boldsymbol{\theta}, \mathbf{p}) \rightarrow (\boldsymbol{\theta}^*, \mathbf{p}^*)$ where

$$\boldsymbol{\theta}^* = \boldsymbol{\theta} + \epsilon m_i^{-1} \text{sign}(p_i) \mathbf{e}_i, \quad \mathbf{p}^* = \mathbf{p} - m_i \{U(\boldsymbol{\theta}^*) - U(\boldsymbol{\theta})\} \mathbf{e}_i \quad (\text{A1})$$

if $U\{\boldsymbol{\theta} + \epsilon m_i^{-1} \text{sign}(p_i) \mathbf{e}_i\} - U(\boldsymbol{\theta}) > m_i^{-1} p_i$, and otherwise

$$\boldsymbol{\theta}^* = \boldsymbol{\theta}, \quad \mathbf{p}^* = -\mathbf{p} \quad (\text{A2})$$

The update equations (A1) and (A2) are well-defined and differentiable except on the measure-zero set S , which we define momentarily. Under both (A1) and (A2), we have $\partial \boldsymbol{\theta}^* / \partial \mathbf{p} = 0$ and can easily show that

$$\det \left\{ \frac{\partial(\boldsymbol{\theta}^*, \mathbf{p}^*)}{\partial(\boldsymbol{\theta}, \mathbf{p})} \right\} = \det \left(\frac{\partial \boldsymbol{\theta}^*}{\partial \boldsymbol{\theta}} \right) \det \left(\frac{\partial \mathbf{p}^*}{\partial \mathbf{p}} \right) = 1, \quad (\text{A3})$$

establishing the volume-preservation. The reversibility as defined in (20) can be directly verified by solving the update equations (A1) and (A2) for $(\boldsymbol{\theta}, -\mathbf{p})$ as a function of $(\boldsymbol{\theta}^*, -\mathbf{p}^*)$.

We now quantify the set S on which the above argument may break down and show that it has measure zero. Let \mathcal{D} denote the discontinuity set of $U(\boldsymbol{\theta})$ and $\mathcal{D} + \mathbf{v}$ denote a set of points in \mathcal{D} shifted by a vector \mathbf{v} . It is easy to see that the update equations (A1) and (A2) are well-defined and differentiable except when $(\boldsymbol{\theta}, \mathbf{p})$ belongs to one of the sets below:

$$\mathcal{D} \times \mathbb{R}^d, \quad (\mathcal{D} \pm \epsilon m_i^{-1} \mathbf{e}_i) \times \mathbb{R}^d, \quad \{p_i = 0\}, \quad \{U\{\boldsymbol{\theta} + \epsilon m_i^{-1} \text{sign}(p_i) \mathbf{e}_i\} - U(\boldsymbol{\theta}) = m_i^{-1} p_i\}. \quad (\text{A4})$$

Each of the sets above consists of lower-dimensional manifolds of the parameter space and hence has measure zero. We now define the set S as the union of all the sets (A4) over $i = 1, \dots, d$. Being a finite union of measure-zero sets, the set S also has measure zero.

Lastly, we prove the reversibility of multiple coordinate updates corresponding to a map $\Psi_{\varphi(d),\epsilon} \circ \dots \circ \Psi_{\varphi(1),\epsilon}$ with a random permutation φ . From the reversibility of each $\Psi_{i,\epsilon}$, we deduce that

$$\mathbf{R} \circ (\Psi_{\varphi(d),\epsilon} \circ \dots \circ \Psi_{\varphi(1),\epsilon}) \circ \mathbf{R} = \Psi_{\varphi(d),\epsilon}^{-1} \circ \dots \circ \Psi_{\varphi(1),\epsilon}^{-1} = (\Psi_{\varphi(1),\epsilon} \circ \dots \circ \Psi_{\varphi(d),\epsilon})^{-1}. \quad (\text{A5})$$

By our assumption on the distribution of φ , we have

$$(\Psi_{\varphi(1),\epsilon} \circ \dots \circ \Psi_{\varphi(d),\epsilon})^{-1} \stackrel{d}{=} (\Psi_{\varphi(d),\epsilon} \circ \dots \circ \Psi_{\varphi(1),\epsilon})^{-1} \quad (\text{A6})$$

establishing the reversibility of $\Psi_{\varphi(d),\epsilon} \circ \dots \circ \Psi_{\varphi(1),\epsilon}$ in distribution. \square

Proof Theorem 1. Let $\Psi_{J,\varphi,\epsilon} = \Psi_{\varphi(d'),\epsilon} \circ \dots \circ \Psi_{\varphi(1),\epsilon}$ where $\Psi_{j,\epsilon} : (\boldsymbol{\theta}, \mathbf{p}) \rightarrow (\boldsymbol{\theta}^*, \mathbf{p}^*)$ is defined as in (A1) and (A2) and $\varphi(1), \dots, \varphi(d')$ is a permutation of the indexing set J . Also define $\Psi_{\Theta, I, \epsilon/2}$ and $\Psi_{P, I, \epsilon/2}$ as a function of $(\boldsymbol{\theta}, \mathbf{p})$ such that

$$\Psi_{\Theta, I, \epsilon/2} : \boldsymbol{\theta}_I \rightarrow \boldsymbol{\theta}_I + \frac{\epsilon}{2} \mathbf{M}_I^{-1} \mathbf{p}_I, \quad \Psi_{P, I, \epsilon/2} : \mathbf{p}_I \rightarrow \mathbf{p}_I - \frac{\epsilon}{2} \nabla_{\boldsymbol{\theta}_I} U(\boldsymbol{\theta}) \quad (\text{A7})$$

while leaving all the other coordinates unchanged. The integrator of Algorithm 2 can then be formally expressed as a map

$$\Psi_{\Theta, I, \epsilon/2} \circ \Psi_{P, I, \epsilon/2} \circ \Psi_{J, \varphi, \epsilon} \circ \Psi_{P, I, \epsilon/2} \circ \Psi_{\Theta, I, \epsilon/2} \quad (\text{A8})$$

Being a symmetric composition of reversible maps, the map (A8) is again reversible. The maps $\Psi_{\Theta, I, \epsilon/2} \circ \Psi_{P, I, \epsilon/2}$ and $\Psi_{P, I, \epsilon/2} \circ \Psi_{\Theta, I, \epsilon/2}$ coincide with symplectic Euler schemes in the coordinate (θ_I, p_I) and hence are volume preserving (Hairer et al., 2006). Since $\Psi_{J, \varphi, \epsilon}$ is also volume-preserving by the results of Lemma 1, the composition (A8) is volume-preserving. \square

REFERENCES

- AFSHAR, H. M. & DOMKE, J. (2015). Reflection, refraction, and Hamiltonian Monte Carlo. In *Proceedings of the 28th International Conference on Neural Information Processing Systems*.
- AMBROSIO, L. (2008). Transport equation and cauchy problem for non-smooth vector fields. In *Calculus of variations and nonlinear partial differential equations*. Springer, pp. 1–41.
- ANDRIEU, C. & THOMS, J. (2008). A tutorial on adaptive MCMC. *Statistics and Computing* **18**, 343–373.
- BERGER, J. O., BERNARDO, J. M. & SUN, D. (2012). Objective priors for discrete parameter spaces. *Journal of the American Statistical Association* **107**, 636–648.
- BESKOS, A., PILLAI, N., ROBERTS, G., SANZ-SERNA, J.-M. & STUART, A. (2013). Optimal tuning of the hybrid Monte Carlo algorithm. *Bernoulli* **19**, 1501–1534.
- BETANCOURT, M., BYRNE, S. & GIROLAMI, M. (2014). Optimizing the integrator step size for Hamiltonian Monte Carlo. *arXiv:1411.6669*.
- BIERKENS, J., BOUCHARD-CÔTÉ, A., DOUCET, A., DUNCAN, A. B., FEARNHEAD, P., ROBERTS, G. & VOLLMER, S. J. (2017). Piecewise deterministic Markov processes for scalable Monte Carlo on restricted domains. *arXiv:1701.04244*.
- BIERKENS, J., FEARNHEAD, P. & ROBERTS, G. (2016). The zig-zag process and super-efficient sampling for Bayesian analysis of big data. *arXiv:1607.03188*.
- BISSIRI, P. G., HOLMES, C. C. & WALKER, S. G. (2016). A general framework for updating belief distributions. *Journal of the Royal Statistical Society: Series B (Statistical Methodology)* **78**, 1103–1130.
- CARPENTER, B., HOFFMAN, M. D., BRUBAKER, M., LEE, D., LI, P. & BETANCOURT, M. (2015). The Stan math library: Reverse-mode automatic differentiation in C++. *arXiv:1509.07164*.
- CARVALHO, C. M., POLSON, N. G. & SCOTT, J. G. (2010). The horseshoe estimator for sparse signals. *Biometrika* **97**, 465–480.
- CHIB, S. (1998). Estimation and comparison of multiple change-point models. *Journal of Econometrics* **86**, 221–241.
- CHOPIN, N. & RIDGWAY, J. (2017). Leave Pima indians alone: binary regression as a benchmark for Bayesian computation. *Statistical Science* **32**, 64–87.
- DINH, V., BILGE, A., ZHANG, C. & MATSEN, F. A. (2017). Probabilistic path Hamiltonian Monte Carlo. *arXiv:1702.07814*.
- DUANE, S., KENNEDY, A. D., PENDLETON, B. J. & ROWETH, D. (1987). Hybrid Monte Carlo. *Physics Letters B* **195**, 216–222.
- FANG, Y., SANZ-SERNA, J. M. & SKEEL, R. D. (2014). Compressible generalized hybrid Monte Carlo. *The Journal of Chemical Physics* **140**, 174108.
- FEARNHEAD, P., BIERKENS, J., POLLOCK, M. & ROBERTS, G. O. (2016). Piecewise deterministic Markov processes for continuous-time Monte Carlo. *arXiv:1611.07873*.
- FRYZLEWICZ, P. & SUBBA RAO, S. (2014). Multiple-change-point detection for auto-regressive conditional heteroscedastic processes. *Journal of the Royal Statistical Society: Series B (Statistical Methodology)* **76**, 903–924.
- GELMAN, A. (2006). Prior distributions for variance parameters in hierarchical models. *Bayesian Analysis* **1**, 515–534.
- GELMAN, A., CARLIN, J. B., STERN, H. S., DUNSON, D. B., VEHTARI, A. & RUBIN, D. B. (2013). *Bayesian Data Analysis*. CRC Press.
- GELMAN, A., LEE, D. & GUO, J. (2015). Stan: a probabilistic programming language for Bayesian inference and optimization. *Journal of Educational and Behavior Science* **40**, 530–543.
- GELMAN, A., ROBERTS, G. O. & GILKS, W. R. (1996). Efficient Metropolis jumping rules. *Bayesian Statistics* **5**, 599–607.
- GEYER, C. (2011). Introduction to Markov chain Monte Carlo. *Handbook of Markov Chain Monte Carlo*, 3–48.
- GIROLAMI, M. & CALDERHEAD, B. (2011). Riemann manifold Langevin and Hamiltonian Monte Carlo methods. *Journal of the Royal Statistical Society: Series B (Statistical Methodology)* **73**, 123–214.
- GRAM-HANSEN, B., ZHOU, Y., KOHN, T., YANG, H. & WOOD, F. (2018). Discontinuous Hamiltonian Monte Carlo for probabilistic programs. *arXiv:1804.03523*.

- GRIEWANK, A. & WALTHER, A. (2008). *Evaluating derivatives: principles and techniques of algorithmic differentiation*. Society for Industrial and Applied Mathematics.
- HAARIO, H., SAKSMAN, E. & TAMMINEN, J. (2001). An adaptive metropolis algorithm. *Bernoulli* , 223–242.
- HAARIO, H., SAKSMAN, E. & TAMMINEN, J. (2005). Componentwise adaptation for high dimensional MCMC. *Computational Statistics* **20**, 265–273.
- HAIRER, E., LUBICH, C. & WANNER, G. (2006). *Geometric Numerical Integration. Structure-Preserving Algorithms for Ordinary Differential Equations*. Springer-Verlag.
- HOFFMAN, M. D. & GELMAN, A. (2014). The no-U-turn sampler: adaptively setting path lengths in Hamiltonian Monte Carlo. *Journal of Machine Learning Research* **15**, 1593–1623.
- JOHNSON, A. A., JONES, G. L. & NEATH, R. C. (2013). Component-wise Markov chain Monte Carlo: Uniform and geometric ergodicity under mixing and composition. *Statistical Science* , 360–375.
- JOLLY, G. M. (1965). Explicit estimates from capture-recapture data with both death and immigration-stochastic model. *Biometrika* **52**, 225–247.
- KRUSCHKE, J. (2014). *Doing Bayesian Data Analysis, Second Edition: A Tutorial with R, JAGS, and Stan*. Academic Press.
- LEIMKUHLER, B. & REICH, S. (2005). *Simulating Hamiltonian Dynamics*. Cambridge University Press.
- LIVINGSTONE, S., BETANCOURT, M., BYRNE, S. & GIROLAMI, M. (2016). On the geometric ergodicity of Hamiltonian Monte Carlo. *arXiv:1601.08057* .
- LU, X., PERRONE, V., HASENCLEVER, L., TEH, Y. W. & VOLLMER, S. J. (2016). Relativistic Monte Carlo. *arXiv:1609.04388* .
- LUNN, D., SPIEGELHALTER, D., THOMAS, A. & BEST, N. (2009). The BUGS project: Evolution, critique and future directions. *Statistics in medicine* **28**, 3049–3067.
- MCLACHLAN, R. I. & QUISP, G. R. W. (2002). Splitting methods. *Acta Numerica* **11**, 341–434.
- METROPOLIS, N., ROSENBLUTH, A. W., ROSENBLUTH, M. N., TELLER, A. H. & TELLER, E. (1953). Equation of state calculations by fast computing machines. *The Journal of Chemical Physics* **21**, 1087–1092.
- MONNAHAN, C. C., THORSON, J. T. & BRANCH, T. A. (2016). Faster estimation of Bayesian models in ecology using Hamiltonian Monte Carlo. *Methods in Ecology and Evolution* , 339–348.
- NAKAJIMA, J. & WEST, M. (2013). Bayesian analysis of latent threshold dynamic models. *Journal of Business & Economic Statistics* **31**, 151–164.
- NEAL, R. M. (1996). *Bayesian Learning for Neural Networks*. Springer-Verlag.
- NEAL, R. M. (2010). MCMC using Hamiltonian Dynamics. In *Handbook of Markov chain Monte Carlo*. CRC Press.
- NEELON, B. & DUNSON, D. B. (2004). Bayesian isotonic regression and trend analysis. *Biometrics* **60**, 398–406.
- NISHIMURA, A. & DUNSON, D. (2015). Recycling intermediate steps to improve Hamiltonian Monte Carlo. *arXiv:1511.06925* .
- PAKMAN, A. & PANINSKI, L. (2013). Auxiliary-variable exact Hamiltonian Monte Carlo samplers for binary distributions. In *Proceedings of the 26th International Conference on Neural Information Processing Systems*.
- PETERS, E. A. J. F. & DE WIT, G. (2012). Rejection-free Monte Carlo sampling for general potentials. *Physical Review E* **85**, 026703.
- ROBERTS, G. O., GELMAN, A. & GILKS, W. R. (1997). Weak convergence and optimal scaling of random walk Metropolis algorithms. *The Annals of Applied Probability* **7**, 110–120.
- ROBERTS, G. O. & ROSENTHAL, J. S. (2009). Examples of adaptive MCMC. *Journal of Computational and Graphical Statistics* **18**, 349–367.
- SALVATIER, J., WIECKI, T. V. & FONNESBECK, C. (2016). Probabilistic programming in Python using PyMC3. *PeerJ Computer Science* .
- SCHWARZ, C. J. & ARNASON, A. N. (1996). A general methodology for the analysis of capture-recapture experiments in open populations. *Biometrics* , 860–873.
- SCHWARZ, C. J. & SEBER, G. A. F. (1999). Estimating animal abundance: Review III. *Statistical Science* **14**, 427–456.
- SEBER, G. A. F. (1982). *The estimation of animal abundance*. Griffin London.
- STAN DEVELOPMENT TEAM (2016). *Stan Modeling Language Users Guide and Reference Manual, Version 2.14.0*.
- STEWART, D. E. (2000). Rigid-body dynamics with friction and impact. *SIAM Review* **42**, 3–39.
- THAWORNWATTANA, Y., DALQUEN, D., YANG, Z. et al. (2018). Designing simple and efficient Markov chain Monte Carlo proposal kernels. *Bayesian Analysis* .
- WAGNER, A. K., SOUMERAI, STEPHEN B. AND ZHANG, F. & ROSS-DEGNAN, D. (2002). Segmented regression analysis of interrupted time series studies in medication use research. *Journal of Clinical Pharmacy and Therapeutics* **27**, 299–309.
- ZHANG, Y., SUTTON, C., STORKEY, A. & GHAHRAMANI, Z. (2012). Continuous relaxations for discrete Hamiltonian Monte Carlo. In *Proceedings of the 25th International Conference on Neural Information Processing Systems*.
- ZHANG, Y., WANG, X., CHEN, C., HENAO, R., FAN, K. & CARIN, L. (2016). Towards unifying Hamiltonian Monte Carlo and slice sampling. *arXiv:1602.07800* .

Supplement to “Discontinuous Hamiltonian Monte Carlo for discrete parameters and discontinuous likelihoods”

Here we describe an implementation of the integrator proposed by Pakman & Paninski (2013) and Afshar & Domke (2015). The integrator is designed to approximate a discontinuous Hamiltonian dynamics with a Gaussian momentum corresponding to the kinetic energy $K(\mathbf{p}) = \|\mathbf{p}\|^2/2$. For simplicity, we assume that a parameter space θ consists only of the embedded discrete parameters as described in Section 2.2, so that the target $\pi_{\Theta}(\cdot)$ is piecewise constant with the discontinuity set consisting of the boundaries of hyper-cubes. The integrator is energy-preserving in this simplified setting but not so for more general discontinuous dynamics. The pseudo code is given in Algorithm S1.

Algorithm S1. Integrator for Gaussian momentum-based discontinuous dynamics

Input: initial state (θ, \mathbf{p}) , stepsize ϵ

$t \leftarrow 0$

while $t < \epsilon$ **do**

$t_e \leftarrow$ the time until reaching the next discontinuity

if $t + t_e > \epsilon$ **then**

$\theta \leftarrow \theta + (\epsilon - t)\mathbf{p}$

$t \leftarrow \epsilon$

else

$\theta \leftarrow \theta + t_e\mathbf{p}$

$i \leftarrow$ the index of the axis orthogonal to the discontinuity plane at θ

$\Delta U_e \leftarrow$ the potential energy difference

if $p_i^2/2 > \Delta U_e$ **then**

$p_i \leftarrow \sqrt{p_i^2 - 2\Delta U_e}$

else

$p_i \leftarrow -p_i$

$t \leftarrow t + t_e$

S1. EMPIRICAL VERIFICATION OF ERGODICITY AND UNBIASEDNESS OF DISCONTINUOUS HAMILTONIAN MONTE CARLO

To empirically back up the theoretical results of Section 4, here we use discontinuous Hamiltonian Monte Carlo to sample from a simple posterior distribution with closed-form marginal distributions. It is worth mentioning that the correctness of discontinuous Hamiltonian Monte Carlo has also been independently verified by Gram-Hansen et al. (2018), in which the discontinuous Hamiltonian Monte Carlo samples are compared to the outputs of existing probabilistic programming softwares.

We consider an observation model $y | q, N \sim \text{Binomial}(q, N)$ where both the success rate q and sample size N are unknown. We assign an objective prior $\pi(N) \propto N^{-1}$ (Berger et al., 2012) and a beta prior $q \sim \text{Beta}(\alpha, \beta)$. As a particular choice made is immaterial for the purpose of our simulation, we just pick $\alpha = \beta = 2$ and set $y = 100$. Closed-form expressions for the posterior marginals of N and q are given in Section S1.1 below.

To sample from the posterior, we use the log-transformed embedding of N (Section 2.2). The parameter q is mapped to a real line through a logit transform $q \rightarrow \log\{q/(1-q)\}$. We use the integrator of Section 3.4 (Algorithm 2) with the Laplace momentum for N and Gaussian momentum for q . The stepsize ϵ is jittered in the range $[0.08, 0.1]$ and the number of numerical integration steps in the range $[15, 20]$.

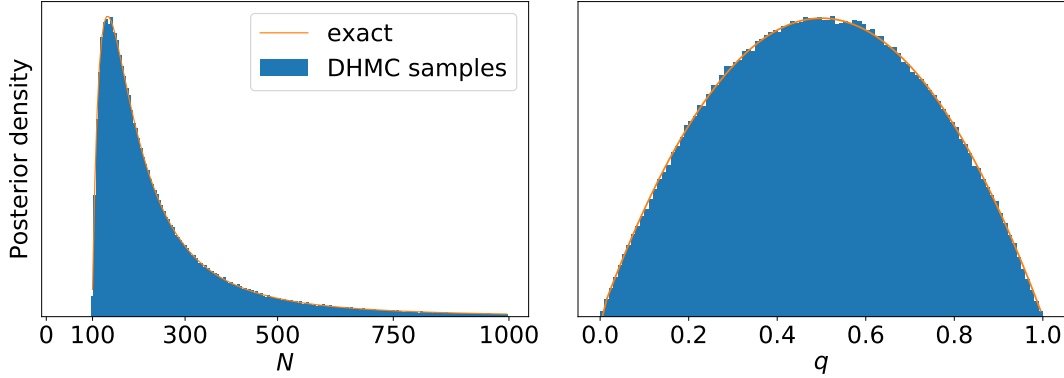


Fig. S1. Empirical distributions of the discontinuous Hamiltonian Monte Carlo samples generated for the target distribution as described in Section S1.1. The orange lines show the exact posterior mass and density functions computed from the closed-form expressions. The unknown sample size parameter N has no posterior probability below the observed number of successes $y = 100$.

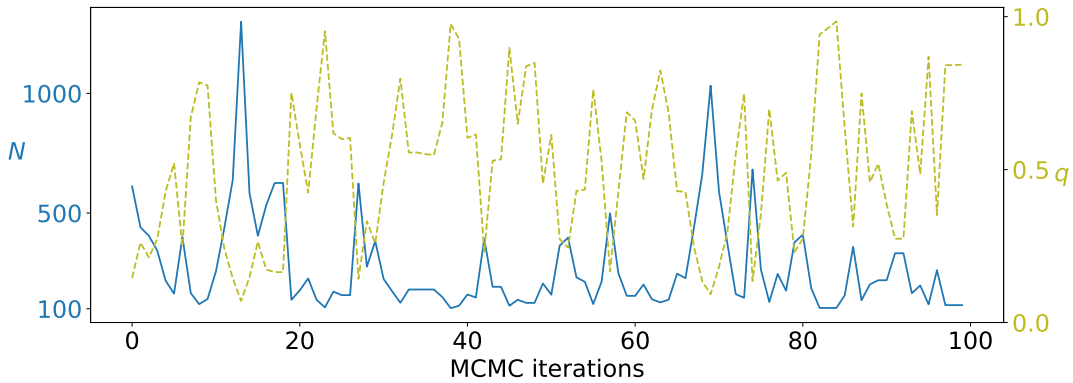


Fig. S2. Trace plots for the first 100 discontinuous Hamiltonian Monte Carlo samples generated for the target distribution as described in Section S1.1. The blue line and left y -axis indicates the parameter values of N , while the olive line and right y -axis indicates the parameter values of q .

Figure S1 shows the empirical distributions of $N|y$ and $q|y$ from 10^6 iterations of discontinuous Hamiltonian Monte Carlo. The empirical distributions are indistinguishable from the exact distributions indicated by the orange lines. Additionally, the trace plot in Figure S2 shows that discontinuous Hamiltonian Monte Carlo can induce a large transition in the parameter N with only a small number of numerical integration steps. This means that the discontinuous Hamiltonian Monte Carlo integrator often jumps through a large number of discontinuities along the parameter N at each numerical integration step. This behavior introduces no bias as the integrator remains reversible and volume-preserving regardless of its stepsize as discussed in the main manuscript Section 4.

S1.1. Derivation of the posterior marginals

For the model and priors described above, we have

$$\pi(N, q | y) \propto \frac{N!}{(N-y)!} q^y (1-q)^{N-y} \pi(q) \pi(N) \propto \frac{(N-1)!}{(N-y)!} q^{y+\alpha-1} (1-q)^{N-y+\beta-1} \quad (\text{S1})$$

Integrating over q , we obtain

$$\pi(N | y) \propto \frac{(N-1)! \Gamma(N-y+\beta)}{(N-y)! \Gamma(N+\alpha+\beta)} = \frac{(N-1)! (N-y+\beta-1)!}{(N-y)! (N+\alpha+\beta-1)!} \quad (\text{S2})$$

where the equality holds when α and β take positive integer values. As a particular choice made is immaterial for the purpose of our simulation, we just pick $\alpha = \beta = 2$ which yields

$$\pi(N | y) \propto \frac{N-y+1}{(N+3)(N+2)(N+1)N} \quad (\text{S3})$$

We can compute the normalized mass function of $N | y$ to high accuracy by truncating it a suitably large number. Having computed $\pi(N | y)$, we can compute the posterior marginal of q via the law of total expectation $\pi(q | y) = \sum_N \pi(q | N, y) \pi(N | y)$ where $q | N, y \sim \text{Beta}(y + \alpha, N - y + \beta)$.

S2. RELATIVE ADVANTAGES OF JOINT AND COORDINATE-WISE UPDATES ON CONTINUOUS PARAMETERS

While the coordinate-wise update of Algorithm 1 in the main manuscript generates a valid proposal whether or not $U(\theta)$ has discontinuities along θ_i , the joint update of continuous parameters as in Algorithm 2 has some computational advantages. First, when there is little conditional independence structure, calculating $\nabla_{\theta_I} U(\theta)$ is more computationally efficient than carrying out $|I|$ successive conditional density evaluations. Even when there is some conditional independence structure, however, computing $\nabla_{\theta_I} U(\theta)$ may still be substantially faster as an interpreter or compiler (of a programming language) can more easily optimize the required computation. Thus the joint update typically demands less computing time. On the other hand, the coordinate-wise updates have an advantage of being rejection-free by virtue of exact energy-preservation. The coordinate-wise update may thus be preferable for posteriors with substantial conditional independence structure such as those in latent Markov random field models.

S3. TUNING MASS MATRIX AND INTEGRATOR STEPSIZE OF DISCONTINUOUS HAMILTONIAN MONTE CARLO

S3.1. Role and tuning of mass matrix

As in the case of traditional Hamiltonian Monte Carlo, using a non-identity mass matrix has the effect of preconditioning a target distribution through reparametrization (Neal, 2010). More precisely, for a matrix \mathbf{A}_I and a diagonal matrix \mathbf{A}_J , the performance of discontinuous Hamiltonian Monte Carlo in a sampling space $(\mathbf{A}_I \theta_I, \mathbf{A}_J \theta_J, \mathbf{p}_I, \mathbf{p}_J)$ is identical to that in $(\theta_I, \theta_J, \mathbf{A}_I^\top \mathbf{p}_I, \mathbf{A}_J^\top \mathbf{p}_J)$. The choice of a mass matrix for a Gaussian momentum is a well-studied topic (Neal, 2010; Girolami & Calderhead, 2011). We can reason similarly for a Laplace momentum. We generally expect that sampling is facilitated by a reparametrization $\theta_j \rightarrow \theta_j / \text{var}(\theta_j)^{1/2}$ for $j \in J$. This is effectively achieved by, given the relation between mass matrix choice and parameter transformation, by choosing the mass to be $m_j \approx \text{var}(\theta_j)^{-1/2}$. The variances can be estimated from a small number of preliminary discontinuous Hamiltonian Monte Carlo iterations.

S3.2. Choice and tuning of integrator stepsize

The stepsize ϵ should be adjusted so that ϵm_j^{-1} has the same order of magnitude as a typical scale of the conditional distribution of θ_j . Unlike a leapfrog integrator that becomes unstable as ϵ increases, the coordinate-wise integrator remains exactly energy-preserving but at some point a large stepsize will cause

discontinuous Hamiltonian Monte Carlo to “get stuck” at the current state. The numerical integration scheme of discontinuous Hamiltonian Monte Carlo will keep flipping the momentum $p_j \leftarrow -p_j$ (Line 9 of Algorithm 1) without updating θ_j until the following condition is met:

$$U\{\boldsymbol{\theta} + \epsilon m_j^{-1} \text{sign}(p_j) \mathbf{e}_j\} - U(\boldsymbol{\theta}) < m_j^{-1} |p_j| \stackrel{d}{=} \text{Exponential}(1) \quad (\text{S1})$$

where \mathbf{e}_j denotes the j -th standard basis vector. When ϵm_j^{-1} becomes larger than a typical scale of θ_j , the condition (S1) becomes unlikely to be satisfied, leading to infrequent updates of θ_j .

We now consider how to tune the stepsize while the mass matrix being fixed. This can be alternated with tuning of the mass matrix as suggested above to calibrate both the tuning parameters. To this end, we propose the following statistics:

$$\begin{aligned} & \mathbb{P}_{\pi_{\Theta} \times \pi_P} [U\{\boldsymbol{\theta} + \epsilon m_j^{-1} \text{sign}(p_j) \mathbf{e}_j\} - U(\boldsymbol{\theta}) > m_j^{-1} |p_j|] \\ & = \mathbb{E}_{\pi_{\Theta} \times \pi_P} \left\{ \min \left(1, \exp \left[U(\boldsymbol{\theta}) - U\{\boldsymbol{\theta} + \epsilon m_j^{-1} \text{sign}(p_j) \mathbf{e}_j\} \right] \right) \right\}. \end{aligned} \quad (\text{S2})$$

The above statistics play a role analogous to the acceptance rate of Metropolis proposals. The statistics (S2) can be estimated, for example, by counting the frequency of momentum flips during each discontinuous Hamiltonian Monte Carlo iteration, and can then be used to tune the stepsize through stochastic optimization (Andrieu & Thoms, 2008; Hoffman & Gelman, 2014). One would want the statistics to be well above zero but not too close to 1, balancing the mixing rate and computational cost of each discontinuous Hamiltonian Monte Carlo iteration. Theoretical analysis of the optimal statistics value is beyond the scope of this paper, but the value $0.7 \sim 0.9$ is perhaps reasonable in analogy with the optimal acceptance rate for Hamiltonian Monte Carlo (Betancourt et al., 2014).

S4. CONNECTIONS BETWEEN ZIG-ZAG PROCESS AND LAPLACE MOMENTUM-BASED HAMILTONIAN DYNAMICS

Zig-zag sampler is a state-of-the-art non-reversible Monte Carlo algorithm based on a piece-wise deterministic Markov process called a *zig-zag process* (Bierkens et al., 2016; Fearnhead et al., 2016; Bierkens et al., 2017). Here we describe a remarkable similarity between a zig-zag process and the Laplace momentum-based Hamiltonian dynamics with unit mass $m_j = 1$.

As described in Section 3.2 of the main manuscript, this Hamiltonian dynamics is governed by the following differential equation:

$$\frac{d\boldsymbol{\theta}}{dt} = \text{sign}(\mathbf{p}), \quad \frac{d\mathbf{p}}{dt} = -\nabla_{\boldsymbol{\theta}} U(\boldsymbol{\theta}) \quad (\text{S1})$$

Consider a zig-zag process and Hamiltonian dynamics both starting from the state $\boldsymbol{\theta}_0$. Let \mathbf{v}_0 drawn uniformly from $\{-1, +1\}^d$ be the initial velocity of the zig-zag process and $\mathbf{p}_0 = (p_{0,1}, \dots, p_{0,d})$ drawn from the independent Laplace distribution be the initial momentum of the Hamiltonian dynamics. Under both the zig-zag process and Hamiltonian dynamics, the velocities remain constant while the parameter $\boldsymbol{\theta}$ moves along a straight line $\boldsymbol{\theta}^Z(t) = \boldsymbol{\theta}_0 + t\mathbf{v}_0$ and $\boldsymbol{\theta}^H(t) = \boldsymbol{\theta}_0 + t \text{sign}(\mathbf{p}_0)$ for $t > 0$ until their respective first event times. The first event time for the zig-zag process is given as $t_e^Z = \min\{t_1^Z, \dots, t_d^Z\}$ where

$$t_i^Z = \inf_{t' > 0} \left\{ \tau_i = \int_0^{t'} [v_{0,i} \partial_{\theta_i} U(\boldsymbol{\theta}_0 + t\mathbf{v}_0)]^+ dt' \right\} \quad (\text{S2})$$

with $[x]^+ = \max\{0, x\}$ and τ_i 's drawn from $\text{Exp}(1)$. For the Hamiltonian dynamics, the first event time is given as $t_e^H = \min\{t_1^H, \dots, t_d^H\}$ where

$$t_i^H = \inf_{t' > 0} \left[|p_{0,i}| = \int_0^{t'} \text{sign}(p_{0,i}) \partial_{\theta_i} U\{\boldsymbol{\theta}_0 + t \text{sign}(\mathbf{p}_0)\} dt' \right] \quad (\text{S3})$$

For both processes, the events result in the velocity change $v_k \leftarrow -v_k$ and $\text{sign}(p_\ell) \leftarrow -\text{sign}(p_\ell)$ for $k = \text{argmin}_i \{t_i^Z\}$ and $\ell = \text{argmin}_i \{t_i^H\}$.

Given that $(\mathbf{v}_0, \boldsymbol{\tau}) \stackrel{d}{=} \{\text{sign}(\mathbf{p}_0), |\mathbf{p}_0|\}$, the similarity between (S2) and (S3) is striking. In fact, if $U(\boldsymbol{\theta})$ were convex and $\boldsymbol{\theta}_0$ was the minimum of $U(\boldsymbol{\theta})$, then the two processes $\{\boldsymbol{\theta}^Z(t), 0 \leq t \leq t_e^Z\}$ and $\{\boldsymbol{\theta}^H(t), 0 \leq t \leq t_e^H\}$ coincide in distribution. After the first event time or in more general settings, however, the two processes diverge because a zig-zag process $(\boldsymbol{\theta}^Z, d\boldsymbol{\theta}^Z/dt) = (\boldsymbol{\theta}^Z, \mathbf{v})$ is Markovian while its Hamiltonian dynamics counter-part $(\boldsymbol{\theta}^H, d\boldsymbol{\theta}^H/dt) = \{\boldsymbol{\theta}^H, \text{sign}(\mathbf{p})\}$ is not. More precisely, Hamiltonian dynamics after each event retains the magnitudes of its momentum $|p_i|$'s from the previous moment, so that the future evolution of $\{\boldsymbol{\theta}^H, \text{sign}(\mathbf{p})\}$ cannot be determined only from its current value without the magnitude information. Also, Hamiltonian dynamics accumulates kinetic energy while going potential energy downhill such that $\text{sign}\{p_i(t)\} \partial_{\theta_i} U\{\boldsymbol{\theta}^H(t)\} < 0$. This creates a tendency for each coordinate of a Hamiltonian dynamics trajectory $\boldsymbol{\theta}^H(t)$ to travel longer in the same direction before switching its direction compared to that of a zig-zag process.

Its close connection to a state-of-the-art sampler partially explains the empirical success of discontinuous Hamiltonian Monte Carlo in Section S6.1, though the application of discontinuous Hamiltonian Monte Carlo to smooth target distributions is outside the main focus of this paper. Some advantages of zig-zag sampler over others have been considered to be its non-reversibility and the fact that its entire trajectory can be used as valid samples from the target. In fact, discontinuous Hamiltonian Monte Carlo can also be made non-reversible through partial momentum refreshments (Neal, 2010) and can utilize the entire trajectories as valid samples (Nishimura & Dunson, 2015). These strategies will likely further boost the performance of discontinuous Hamiltonian Monte Carlo. We will leave further theoretical and empirical comparisons of discontinuous Hamiltonian Monte Carlo and zig-zag sampler to a future work.

S5. ADDITIONAL DETAILS ON JOLLY-SEBER MODEL

S5.1. Sufficient statistics and likelihood function

Under appropriate assumptions, details of which we refer the reader to Seber (1982), the likelihood of the Jolly-Seber model depends only on the following statistics from a capture-recapture experiment carried over $i = 1, \dots, T$ capture occasions:

- R_i = number of marked animals released after the i th capture occasion;
- r_i = number of animals from the released R_i animals that are subsequently captured;
- z_i = number of animals that are caught before i th capture occasion,
not caught in the i th capture occasion, but caught subsequently;
- m_i = number of marked animals caught at the i th capture occasion;
- u_i = number of unmarked animals caught at the i th capture occasion.

The likelihood decomposes into two parts: one for the first captures of previously unmarked animals and another for their re-captures. More precisely,

$$\begin{aligned}
 L(\text{data} | \mathbf{U}, \mathbf{p}, \boldsymbol{\phi}) &= L(\text{first captures}) \times L(\text{re-captures}) \\
 L(\text{first captures}) &\propto \prod_{i=1}^T \frac{U_i!}{U_i - u_i!} p_i^{u_i} (1 - p_i)^{U_i - u_i} \\
 L(\text{re-captures}) &\propto \prod_{i=1}^{T-1} \chi_i^{R_i - r_i} \{\phi_i (1 - p_{i+1})\}^{z_{i+1}} (\phi_i p_{i+1})^{m_{i+1}}
 \end{aligned} \tag{S1}$$

where χ_i represents the conditional probability that a marked animal released after the i th capture occasion is not caught again. Mathematically, χ_i is defined recursively as

$$\chi_{T-1} = 1 - \phi_{T-1} p_T, \quad \chi_i = 1 - \phi_i \{p_{i+1} + (1 - p_{i+1})(1 - \chi_{i+1})\} \tag{S2}$$

S5.2. Prior distribution for $U_{i+1} | U_i, \phi_i$

Let B_i denote the number of “births,” representing animals that are born, enters (immigration), or leaves (emigration) the population after the i th occasion and remains so until the $(i + 1)$ th occasion. Also let S_i denote the number of animals that are unmarked right after the i th capture occasion and survives until the next capture occasion. Then we have $U_{i+1} = B_i + S_i$ where $S_i | U_i, u_i, \phi_i \sim \text{Binomial}(\phi_i, U_i - u_i)$.

The prior distribution of $\{U_i\}_{i=1}^T$ can thus be induced by assigning a prior on B_i ’s. In our example, we assign a convenient prior on U_i ’s based on the assumptions that 1) $\text{Binomial}(\phi_i, U_i - u_i)$ can be approximated by $\mathcal{N}\{U_i - u_i, \phi_i(1 - \phi_i)\}$ and 2) B_i ’s are approximately i.i.d. $\mathcal{N}(0, \sigma_B^2)$. These assumptions motivates a prior

$$U_{i+1} | U_i, u_i, \phi_i, \sigma_B \sim \lfloor \mathcal{N}\{U_i - u_i, \sigma_B^2 + \phi_i(1 - \phi_i)\} \rfloor \quad (\text{S3})$$

where $\lfloor \cdot \rfloor$ is a floor function. We used $\sigma_B = 500$ in our example of Section 5.2 in the main manuscript. An alternative prior on $\{U_i\}_{i=1}^T$ can be assigned to reflect different model and prior assumptions on the number of births. For instance, it is more natural to constrain $B_i \geq 0$ in some cases (Schwarz & Arnason, 1996) and a binomial distribution on B_i will for example induce a Poisson-binomial distribution on the conditional $U_{i+1} | U_i, u_i, \phi_i$ after marginalizing over B_i and S_i .

S5.3. Inference on unknown population sizes

In case the total population sizes $\{N_i\}_{i=1}^T$ at each capture occasion are of interest, we can generate their posterior samples using the relation $N_i = M_i + U_i$ where M_i denotes the number of marked animals right before the $(i + 1)$ th capture occasion. The distribution of $\{M_i\}_{i=1}^T$ follows $M_0 = 0$ and $M_{i+1} | M_i, \phi_i \sim \text{Binomial}(M_i, \phi_i)$.

S6. ADDITIONAL NUMERICAL RESULTS

S6.1. Comparison of discontinuous Hamiltonian Monte Carlo and Gibbs in synthetic example

We use a synthetic target distribution to demonstrate the difference between Metropolis-within-Gibbs with and without momentum as discussed in the main manuscript Section 4.3. While discontinuous Hamiltonian Monte Carlo requires neither conjugacy or smoothness of the conditional densities, we choose a multivariate Gaussian target distribution so that we can compare discontinuous Hamiltonian Monte Carlo to an optimal Metropolis-within-Gibbs implementation with the univariate proposal variances chosen according to the theory of Gelman et al. (1996). In particular, we assume that the target distribution of θ follows that of a stationary unit variance auto-regressive process of the form

$$\theta_t = \alpha\theta_{t-1} + \sqrt{1 - \alpha^2}\eta_t, \quad \theta_1, \eta_t \sim \mathcal{N}(0, 1) \quad (\text{S1})$$

for $t = 2, \dots, 1000$ with $\alpha = 0.9$.

We compare the performances of four algorithms: discontinuous Hamiltonian Monte Carlo (coordinate-wise), Gibbs (full conditional updates), Metropolis-within-Gibbs (univariate updates with optimal proposal variances), and the no-U-turn sampler of Hoffman & Gelman (2014). The performance of each algorithm is summarized in Table S1. Remarkably, discontinuous Hamiltonian Monte Carlo outperforms not only Metropolis-within-Gibbs but also Gibbs, despite requiring no closed-form conditionals at all. After accounting for the computational costs, discontinuous Hamiltonian Monte Carlo improves Gibbs by over 50% and Metropolis-within-Gibbs by over 600%. In general, the advantage of discontinuous Hamiltonian Monte Carlo over Gibbs is expected to increase as the correlations among the parameters increase because the use of momentum can suppress the “random walk behavior” (Neal, 2010). The covariance matrix of the target distribution here has a condition number $\approx 19^2$, which corresponds to a substantial but not particularly severe correlations.

In computing effective sample size per unit time, we estimated theoretical and platform-independent relative computational time of the algorithms as follows. In reasonable low-level language implementations, the computation of conditional densities should account for the majority of computational times

Table S1. Performance summary of each algorithm on the auto-regressive process example. “DHMC” and “ESS” in the table stands for discontinuous Hamiltonian Monte Carlo and effective sample size. The term $(\pm \dots)$ indicates the error estimate of our effective sample size estimators. Path length is averaged over each iteration. “Iter time” shows the computational time for one iteration of each algorithm relative to the fastest one.

	ESS per 100 samples	ESS per unit time	Path length	Iter time
DHMC	77.4 (± 5.2)	7.12	49.5	49.5
No-U-turn	52.4 (± 3.2)	N/A	142	N/A
Gibbs	0.949 (± 0.076)	4.33	N/A	N/A
Metropolis-within-Gibbs	0.219 (± 0.015)	1	N/A	1

for a typical target distribution. Therefore, computational efforts should be roughly equivalent between one numerical integration step of discontinuous Hamiltonian Monte Carlo and one iteration of Metropolis-within-Gibbs sampler. The computational cost of no-U-turn sampler and Gibbs relative to these algorithms is more specific to individual target distributions, depending strongly on specific structures such as conditional independence among the parameters. For this reason, we do not attempt to compare no-U-turn sampler and Gibbs to the other algorithms in terms of effective sample size per unit time.

S6.2. Multiple change-point detection for auto-regressive conditional heteroscedastic processes

Auto-regressive conditional heteroscedastic processes are popular models for log-returns of speculative prices such as stock market indices. A non-stationary first-order auto-regressive conditional heteroscedastic process $\{y_t\}_{t=1}^T$ with parameters $\{a(t), b(t)\}_{t=1}^T$ assumes the distribution

$$y_t | y_{t-1}, a, b \sim \mathcal{N}(0, \sigma_t^2) \quad \text{where } \sigma_t^2 = a(t) + b(t) y_{t-1}^2 \quad (\text{S2})$$

Motivated by its interpretability and advantage in forecasting, Fryzlewicz & Subba Rao (2014) propose a piecewise constant parametrization of $a(t)$ and $b(t)$ as follows:

$$\{a(t), b(t)\} = (a_k, b_k) \quad \text{if } \tau_{k-1} < t \leq \tau_k \quad (\text{S3})$$

for $k = 1, \dots, K$ where the number of change points K and their locations $1 = \tau_0 < \tau_1 < \dots < \tau_K$ are to be estimated along with (a_k, b_k) 's.

To fit the above model within a Bayesian paradigm, we infer the change points through a variable selection type approach as follows, using the horseshoe shrinkage priors of Carvalho et al. (2010). We first choose an upper bound K_{\max} on the number of change points and assume a uniform prior on τ_k 's on the constrained space $1 < \tau_1 < \dots < \tau_{K_{\max}} < T$. We then model the changes in the values of $a(t)$ and $b(t)$ through a prior

$$\begin{aligned} \log(a_k/a_{k-1}) &\sim \mathcal{N}(0, \sigma_a \eta_{a,k}) \\ \log(b_k/b_{k-1}) &\sim \mathcal{N}(0, \sigma_b \eta_{b,k}) \end{aligned} \quad \text{with } \eta_{a,k}, \eta_{b,k} \sim \text{Cauchy}^+(0, 1) \quad (\text{S4})$$

where $\text{Cauchy}^+(0, 1)$ denotes the standard half-Cauchy prior and σ_a and σ_b are the global shrinkage parameters (Carvalho et al., 2010). The above approach can “select” a subset of $\tau_1, \dots, \tau_{K_{\max}}$ as real change points by removing the others through shrinkage $a_k \approx a_{k-1}$ and $b_k \approx b_{k-1}$. We place a default prior $\sigma_a, \sigma_b \sim \text{Cauchy}^+(0, 1)$ for the global shrinkage parameters (Gelman, 2006), and a weak prior $a_0, b_0 \sim \mathcal{N}(0, 1)$ for the initial volatility parameters.

Following Fryzlewicz & Subba Rao (2014), we fit our model to the log-return values of a stock market index over a period that includes the subprime mortgage crisis. In particular, we use the daily closing values of S&P 500 on the market opening days during the period from Jan 1st, 2005 to Dec 31st, 2009. The log-return value cannot be computed when a daily closing value exactly coincides with the previous one; there were four such days during the period and these data points were removed. The model parameters in this example are largely nonidentifiable even with the order constraint $\tau_1, \dots, \tau_{K_{\max}}$. In such cases, it is not clear if the minimum effective sample size across the individual parameters is a good

Table S2. *Performance summary of each algorithm on the change points detection example. “DHMC” and “ESS” in the table stands for discontinuous Hamiltonian Monte Carlo and effective sample size. The term $(\pm \dots)$ is the error estimate of our effective sample size estimators. Path length is averaged over each iteration. “Iter time” shows the computational time for one iteration of each algorithm relative to the fastest one.*

	ESS per 100 samples	ESS per minute	Path length	Iter time
DHMC	13.7 (± 1.1)	38.7	87.3	1.03
No-U-turn / Gibbs	11.6 (± 3.2)	33.5	218	1
No-U-turn / Metropolis	6.04 (± 1.2)	17.5	217	1

measure of efficiency. For this example, therefore, we calculate the minimum effective sample size over the first and second moments of the following quantities: the hyper-parameters σ_a and σ_b , log posterior density, and four summary statistics of the estimated functions $a(t)$ and $b(t)$. The four summary statistics $\log(\|a\|_2)$, $\log(\|b\|_2)$, C_a , and C_b are defined as follows. The quantity $\|a\|_2$ summarizes the deviation of $a(t)$ from its posterior (pointwise empirical) mean $\hat{a}(t)$ and is defined as $\|a\|_2 = \sum_{t=1}^T |a(t) - \hat{a}(t)|^2$. The statistics C_a is a surrogate for the number of “change points” in the function $a(t)$:

$$C_a = |\{k \in \{1, \dots, K_{\max}\} : |\log(a_k/a_{k-1})| > .1\}|. \quad (\text{S5})$$

The statistics $\|b\|_2$ and C_b are defined analogously.

Table S2 summarizes the simulation results; each algorithm is run for 2.5×10^4 starting from stationarity. While No-U-turn / Gibbs and discontinuous Hamiltonian Monte Carlo are comparable in their performances, as discussed earlier discontinuous Hamiltonian Monte Carlo has an advantage that all the necessary computations can be automated within the framework of probabilistic programming languages. For a more useful comparison, therefore, we also implement the default sampling scheme used by PyMC. The algorithm updates each of the discrete parameter via a Metropolis step whose proposal distribution is a symmetric uniform integer-valued distribution with the variance calibrated to achieve the acceptance rate around 40%.

This example is challenging for discontinuous Hamiltonian Monte Carlo as the posterior of τ_k 's are in general multi-modal conditionally on the continuous parameters. The complex dependency between the local shrinkage and the other parameters creates potential paths among the modes, however. It seems that discontinuous Hamiltonian Monte Carlo can exploit this complex posterior geometry efficiently and be competitive with No-U-turn / Gibbs. Figure S3 plots 100 discontinuous Hamiltonian Monte Carlo posterior samples of the piecewise constant volatility functions $a(t)$ and $b(t)$ to illustrate the posterior structure of the model.

S7. SYMPLECTICITY OF DISCONTINUOUS HAMILTONIAN DYNAMICS

Here we establish the *symplecticity* of discontinuous Hamiltonian dynamics under the assumption of Theorem 2. Symplecticity implies a volume preservation and further has important consequences in the stability of numerical approximation schemes (Hairer et al., 2006).

DEFINITION A1. A differentiable map $(\boldsymbol{\theta}, \mathbf{p}) \rightarrow (\boldsymbol{\theta}^*, \mathbf{p}^*)$ is called *symplectic* if

$$\frac{\partial(\boldsymbol{\theta}^*, \mathbf{p}^*)^T}{\partial(\boldsymbol{\theta}, \mathbf{p})} \mathbf{J} \frac{\partial(\boldsymbol{\theta}^*, \mathbf{p}^*)}{\partial(\boldsymbol{\theta}, \mathbf{p})} = \mathbf{J} \quad \text{for } \mathbf{J} = \begin{bmatrix} 0 & \mathbf{I}_d \\ -\mathbf{I}_d & 0 \end{bmatrix} \quad (\text{S1})$$

where \mathbf{I}_d denotes a d -dimensional identity matrix. A dynamics is called symplectic if its solution operator is.

Proof of Theorem 2. Reversibility is a standard property of smooth Hamiltonian dynamics with a symmetric kinetic energy (Hairer et al., 2006). Defined as a point-wise limit of smooth dynamics, discontinuous dynamics therefore is also reversible.

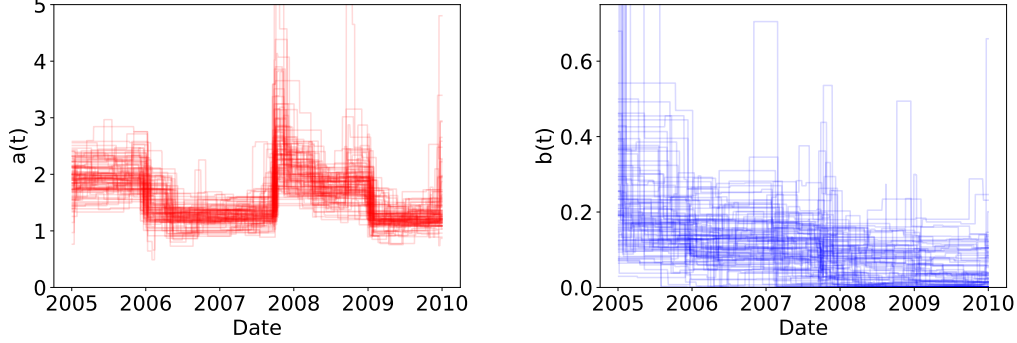


Fig. S3. Posterior samples of the piecewise constant volatility functions $a(t)$ and $b(t)$ from 100 iterations of discontinuous Hamiltonian Monte Carlo.

We turn to the proof of symplecticity. Under the assumption of Theorem 2, the evolution of discontinuous Hamiltonian dynamics from a state $(\boldsymbol{\theta}, \mathbf{p})$ at $t = 0$ to $(\boldsymbol{\theta}^*, \mathbf{p}^*)$ at $t = \tau$ is given as follows. Dividing up the time intervals into a smaller pieces if necessary, we can without loss of generality assume that a trajectory $\{\boldsymbol{\theta}(t), \mathbf{p}(t)\}$ encounters only one discontinuity at $\boldsymbol{\theta}(t_e)$ during the interval $[0, \tau]$. Since $U(\boldsymbol{\theta})$ is piecewise constant, the momentum remains constant and $\boldsymbol{\theta}(t)$ travels in a straight line except when hitting the discontinuity. The relationship between $(\boldsymbol{\theta}, \mathbf{p})$ and $(\boldsymbol{\theta}^*, \mathbf{p}^*)$ is therefore given by

$$\begin{aligned}\boldsymbol{\theta}^* &= \boldsymbol{\theta} + t_e \nabla_{\mathbf{p}} K(\mathbf{p}) + (\tau - t_e) \nabla_{\mathbf{p}} K(\mathbf{p}^*) \\ \mathbf{p}^* &= \mathbf{p} + \gamma(\mathbf{p}) \boldsymbol{\nu}_e\end{aligned}\tag{S2}$$

where $\gamma(\mathbf{p})$ is defined implicitly as a solution of the following relations. If ΔU_e defined as in (8) satisfies $\Delta U_e < K(\mathbf{p}) - \min_c K(\mathbf{p} - c\boldsymbol{\nu}_e)$, we define $\gamma(\mathbf{p})$ as a solution of

$$K(\mathbf{p} - \gamma\boldsymbol{\nu}_e) = K(\mathbf{p}) + \Delta U_e \quad \text{with } \gamma > 0.\tag{S3}$$

Otherwise, $\gamma(\mathbf{p})$ is defined through the relation:

$$K(\mathbf{p} - \gamma\boldsymbol{\nu}_e) = K(\mathbf{p}) \quad \text{with } \gamma > 0\tag{S4}$$

The uniqueness of solutions to the above relations is guaranteed by the convexity and growth condition on $K(\mathbf{p})$, and hence $\gamma(\mathbf{p})$ is well-defined. The event time t_e is also a function of $(\boldsymbol{\theta}, \mathbf{p})$ and can easily shown to be

$$t_e(\boldsymbol{\theta}, \mathbf{p}) = \frac{\alpha - \langle \boldsymbol{\theta}, \boldsymbol{\nu}_e \rangle}{\langle \nabla_{\mathbf{p}} K(\mathbf{p}), \boldsymbol{\nu}_e \rangle}\tag{S5}$$

where α is the distance from the origin of the discontinuity plane of U at $\boldsymbol{\theta}(t_e)$. Assuming that $\boldsymbol{\theta}(t_e)$ is not at the intersection of the linear discontinuity planes and that $\Delta U_e \neq K(\mathbf{p}) - \min_c K(\mathbf{p} - c\boldsymbol{\nu}_e)$, the relation (S2) correctly describes the evolution of the dynamics on a neighborhood of $(\boldsymbol{\theta}, \mathbf{p})$ with $\gamma(\mathbf{p})$ defined either through (S3) or (S4). The map $(\boldsymbol{\theta}, \mathbf{p}) \rightarrow (\boldsymbol{\theta}^*, \mathbf{p}^*)$ therefore is differentiable and Lemma A1 establishes the symplecticity through direct computation.

Lastly, we turn to the almost everywhere differentiability of discontinuous Hamiltonian dynamics. To characterize where the solution operator fails to be differentiable, we first define the following sets:

$$\begin{aligned}\mathcal{D} &= \{ \boldsymbol{\theta} : \text{multiple discontinuity boundaries of } U \text{ intersects at } \boldsymbol{\theta} \}; \\ \mathcal{U} &= \{ \Delta > 0 : \Delta = U(\boldsymbol{\theta}) - U(\boldsymbol{\theta}') \text{ for some } \boldsymbol{\theta}, \boldsymbol{\theta}' \}; \\ \mathcal{V} &= \{ \boldsymbol{\nu} : \boldsymbol{\nu} \text{ is orthonormal to a discontinuity boundary of } U \}.\end{aligned}$$

The above sets are all countable by our assumption on $U(\boldsymbol{\theta})$. Based on the behavior of a trajectory as described in the previous paragraph, a trajectory from the initial state $(\boldsymbol{\theta}_0, \mathbf{p}_0)$ potentially experiences a non-differentiable behavior at time t only if the initial state belongs to one of the sets below:

$$\bigcup_{\boldsymbol{\theta} \in \mathcal{D}} \{(\boldsymbol{\theta} + s \nabla_{\mathbf{p}} K(\mathbf{p}), \mathbf{p}) : s \in \mathbb{R}\}, \quad \bigcup_{\Delta \in \mathcal{U}, \boldsymbol{\nu} \in \mathcal{V}} \left\{ (\boldsymbol{\theta}, \mathbf{p}) : K(\mathbf{p}) - \min_c K(\mathbf{p} - c\boldsymbol{\nu}) = \Delta \right\} \\ \left\{ (\boldsymbol{\theta}, \mathbf{p}) : t = \frac{\alpha - \langle \boldsymbol{\theta}, \boldsymbol{\nu}_e \rangle}{\langle \nabla_{\mathbf{p}} K(\mathbf{p}), \boldsymbol{\nu}_e \rangle} \right\} \quad (\text{S6})$$

Being a countable union of lower dimensional manifolds, the sets above all have measure zero. \square

LEMMA A1. *The map (S2) is symplectic for $\gamma(\mathbf{p})$ and $t_e(\boldsymbol{\theta}, \mathbf{p})$ as defined through (S3), (S4), and (S5).*

Proof. To simplify expressions, we denote $\mathbf{w} = \nabla_{\mathbf{p}} K(\mathbf{p})$, $\mathbf{w}^* = \nabla_{\mathbf{p}} K(\mathbf{p}^*)$, and let \mathcal{H} and \mathcal{H}^* denote the Hessians of K at \mathbf{p} and \mathbf{p}^* . First, an implicit differentiation of either (S3) or (S4) with some algebra yields

$$\frac{\partial \gamma}{\partial \mathbf{p}} = \frac{\mathbf{w}^\top - \mathbf{w}^{*\top}}{\langle \mathbf{w}^*, \boldsymbol{\nu} \rangle} \quad (\text{S7})$$

Differentiating (S2) with respect to $(\boldsymbol{\theta}, \mathbf{p})$, we obtain

$$\frac{\partial \boldsymbol{\theta}^*}{\partial \boldsymbol{\theta}} = \mathbf{I} - \frac{(\mathbf{w} - \mathbf{w}^*) \boldsymbol{\nu}_e^\top}{\langle \mathbf{w}, \boldsymbol{\nu}_e \rangle}, \quad \frac{\partial \boldsymbol{\theta}^*}{\partial \mathbf{p}} = t_e \mathcal{H} - \frac{t_e}{\langle \mathbf{w}, \boldsymbol{\nu}_e \rangle} (\mathbf{w} - \mathbf{w}^*) \boldsymbol{\nu}_e^\top \mathcal{H} + (\tau - t_e) \mathcal{H}^* \frac{\partial \mathbf{p}^*}{\partial \mathbf{p}} \\ \frac{\partial \mathbf{p}^*}{\partial \boldsymbol{\theta}} = 0, \quad \frac{\partial \mathbf{p}^*}{\partial \mathbf{p}} = \mathbf{I} + \frac{\boldsymbol{\nu}_e (\mathbf{w} - \mathbf{w}^*)^\top}{\langle \mathbf{w}^*, \boldsymbol{\nu}_e \rangle} \quad (\text{S8})$$

When $\partial \mathbf{p}^* / \partial \boldsymbol{\theta} = \mathbf{0}$, the symplecticity condition (S1) simplifies to:

$$\frac{\partial \boldsymbol{\theta}^{*\top}}{\partial \boldsymbol{\theta}} \frac{\partial \mathbf{p}^*}{\partial \mathbf{p}} = \mathbf{I}, \quad \frac{\partial \mathbf{p}^{*\top}}{\partial \mathbf{p}} \frac{\partial \boldsymbol{\theta}^*}{\partial \mathbf{p}} = \left(\frac{\partial \mathbf{p}^{*\top}}{\partial \mathbf{p}} \frac{\partial \boldsymbol{\theta}^*}{\partial \mathbf{p}} \right)^\top \quad (\text{S9})$$

The first equality in (S9) is easily verified from (S8). To establish the second equality of (S9), we need to verify the symmetry of the matrix

$$\frac{\partial \mathbf{p}^{*\top}}{\partial \mathbf{p}} \frac{\partial \boldsymbol{\theta}^*}{\partial \mathbf{p}} = t_e \frac{\partial \mathbf{p}^{*\top}}{\partial \mathbf{p}} \left\{ \mathbf{I} - \frac{(\mathbf{w} - \mathbf{w}^*) \boldsymbol{\nu}_e^\top}{\langle \mathbf{w}, \boldsymbol{\nu}_e \rangle} \right\} \mathcal{H} + (\tau - t_e) \frac{\partial \mathbf{p}^{*\top}}{\partial \mathbf{p}} \mathcal{H}^* \frac{\partial \mathbf{p}^*}{\partial \mathbf{p}} \quad (\text{S10})$$

The first term of (S10) simplifies to $t_e \mathcal{H}$, which is symmetric, and the second term is obviously symmetric. \square

S8. ERROR ANALYSIS OF DISCONTINUOUS HAMILTONIAN MONTE CARLO INTEGRATOR

Here we analyze the approximation error incurred by the integrator of Algorithm 2. We focus on the error in Hamiltonian, the amount by which the Hamiltonian fluctuates along a numerical solution, as it determines the acceptance probability of a proposal. An error incurred by one numerical integration step $(\boldsymbol{\theta}^0, \mathbf{p}^0) \rightarrow (\boldsymbol{\theta}^1, \mathbf{p}^1)$ of stepsize ϵ is known as a *local error*. Approximating the evolution $\{\boldsymbol{\theta}(0), \mathbf{p}(0)\} \rightarrow \{\boldsymbol{\theta}(\tau), \mathbf{p}(\tau)\}$ requires $L(\epsilon) = \lfloor \tau/\epsilon \rfloor$ numerical integration steps and the error incurred by the map $(\boldsymbol{\theta}^0, \mathbf{p}^0) \rightarrow (\boldsymbol{\theta}^L, \mathbf{p}^L)$ is known as a *global error*. We quantify the local error of Algorithm 2 in Section S8.1 and relate it to the global error in Section S8.2.

S8.1. Local error in Hamiltonian

In analyzing Algorithm 2, it is useful to break up the algorithm into three steps; the first (partial) update of continuous parameters, the update of discontinuous parameters, and the second update of continuous parameters. The notation $(\boldsymbol{\theta}_I^{1/2}, \mathbf{p}_I^{1/2})$ will refer to the intermediate state after the first update of continuous parameters i.e. $\mathbf{p}_I^{1/2} = \mathbf{p}_I^0 - \frac{\epsilon}{2} \nabla_{\boldsymbol{\theta}_I} U(\boldsymbol{\theta}_I^0, \boldsymbol{\theta}_J^0)$ and $\boldsymbol{\theta}_I^{1/2} = \boldsymbol{\theta}_I^0 + \frac{\epsilon}{2} \nabla_{\mathbf{p}_I} K(\mathbf{p}_I^{1/2}, \mathbf{p}_J^0)$ where $K(\mathbf{p}) = \frac{1}{2} \mathbf{p}_I^\top \mathbf{M}_I^{-1} \mathbf{p}_I + \sum_{j \in J} m_j^{-1} |p_j|$ as before. The update $(\boldsymbol{\theta}_I^0, \mathbf{p}_I^0) \rightarrow (\boldsymbol{\theta}_I^{1/2}, \mathbf{p}_I^{1/2})$ is followed by the

update $(\boldsymbol{\theta}_J^0, \mathbf{p}_J^0) \rightarrow (\boldsymbol{\theta}_J^1, \mathbf{p}_J^1)$ of discontinuous parameters, which then is followed by another continuous parameter update $(\boldsymbol{\theta}_I^{1/2}, \mathbf{p}_I^{1/2}) \rightarrow (\boldsymbol{\theta}_I^1, \mathbf{p}_I^1)$. The exact solution is denoted by $\{\boldsymbol{\theta}(t), \mathbf{p}(t)\}$ with the initial condition $\{\boldsymbol{\theta}(0), \mathbf{p}(0)\} = (\boldsymbol{\theta}^0, \mathbf{p}^0)$.

The key result in this section is Corollary A1 below, which follows immediately from the following theorem:

THEOREM A1. *The local error in Hamiltonian incurred by Algorithm 2 is given by*

$$H(\boldsymbol{\theta}^1, \mathbf{p}^1) - H(\boldsymbol{\theta}^0, \mathbf{p}^0) = \frac{\epsilon^2}{8} \{ \xi(\boldsymbol{\theta}_I^{1/2}, \boldsymbol{\theta}_J^1, \mathbf{p}_I^{1/2}) - \xi(\boldsymbol{\theta}_I^{1/2}, \boldsymbol{\theta}_J^0, \mathbf{p}_I^{1/2}) \} + O(\epsilon^3) \quad (\text{S1})$$

where ξ is defined in terms of the Hessians $\mathcal{I}_U = \partial^2 U / \partial \boldsymbol{\theta}_I^2$ and $\mathcal{I}_K = \partial^2 K / \partial \mathbf{p}_I^2$ (with respect to continuous parameters) as

$$\begin{aligned} \xi(\boldsymbol{\theta}_I, \boldsymbol{\theta}_J, \mathbf{p}_I) &= \nabla_{\boldsymbol{\theta}_I}^\top U(\boldsymbol{\theta}_I, \boldsymbol{\theta}_J) \mathcal{I}_K(\mathbf{p}_I) \nabla_{\boldsymbol{\theta}_I} U(\boldsymbol{\theta}_I, \boldsymbol{\theta}_J) \\ &\quad - \nabla_{\mathbf{p}_I}^\top K(\mathbf{p}_I) \mathcal{I}_U(\boldsymbol{\theta}_I, \boldsymbol{\theta}_J) \nabla_{\mathbf{p}_I} K(\mathbf{p}_I) \end{aligned} \quad (\text{S2})$$

As they are independent of \mathbf{p}_J , the derivatives of K with respect to \mathbf{p}_I are written simply as a function of \mathbf{p}_I in the expression above.

COROLLARY A1. *The local error in Hamiltonian incurred by Algorithm 2 is $O(\epsilon^3)$ when there is no discontinuity of U along the line connecting $\boldsymbol{\theta}_J^0$ and $\boldsymbol{\theta}_J^1$. Otherwise, the local error is $O(\epsilon^2)$.*

Proof of Corollary A1. When there is no discontinuity of U along the line connecting $\boldsymbol{\theta}_J^0$ and $\boldsymbol{\theta}_J^1$, the Taylor expansion of ξ as defined in (S2) with respect to $\boldsymbol{\theta}_J$ implies that

$$\xi(\boldsymbol{\theta}_I^{1/2}, \boldsymbol{\theta}_J^1, \mathbf{p}_I^{1/2}) - \xi(\boldsymbol{\theta}_I^{1/2}, \boldsymbol{\theta}_J^0, \mathbf{p}_I^{1/2}) = O(\|\boldsymbol{\theta}_J^1 - \boldsymbol{\theta}_J^0\|) = O(\epsilon) \quad (\text{S3})$$

So the leading order term of (S1) becomes $O(\epsilon^3)$. \square

Proof of Theorem A1. The update $(\boldsymbol{\theta}_J^0, \mathbf{p}_J^0) \rightarrow (\boldsymbol{\theta}_J^1, \mathbf{p}_J^1)$ is energy-preserving by the property of the coordinate-wise integrator, so we have

$$\begin{aligned} H(\boldsymbol{\theta}^1, \mathbf{p}^1) - H(\boldsymbol{\theta}^0, \mathbf{p}^0) \\ = H(\boldsymbol{\theta}^1, \mathbf{p}^1) - H(\boldsymbol{\theta}_I^{1/2}, \boldsymbol{\theta}_J^1, \mathbf{p}_I^{1/2}, \mathbf{p}_J^1) + H(\boldsymbol{\theta}_I^{1/2}, \boldsymbol{\theta}_J^0, \mathbf{p}_I^{1/2}, \mathbf{p}_J^0) - H(\boldsymbol{\theta}^0, \mathbf{p}^0) \end{aligned} \quad (\text{S4})$$

Now let $(\boldsymbol{\theta}_I^0(t), \mathbf{p}_I^0(t))$ denote the solution of the differential equation

$$\frac{d\boldsymbol{\theta}_I}{dt} = \nabla_{\mathbf{p}_I} K(\mathbf{p}_I, \mathbf{p}_J^0), \quad \frac{d\mathbf{p}_I}{dt} = -\nabla_{\boldsymbol{\theta}_I} U(\boldsymbol{\theta}_I, \boldsymbol{\theta}_J^0) \quad (\text{S5})$$

with the initial condition $\{\boldsymbol{\theta}_I^0(0), \mathbf{p}_I^0(0)\} = (\boldsymbol{\theta}_I^0, \mathbf{p}_I^0)$. Similarly, let $\{\boldsymbol{\theta}_I^{1/2}(t), \mathbf{p}_I^{1/2}(t)\}$ denote the solution of the differential equation

$$\frac{d\boldsymbol{\theta}_I}{dt} = \nabla_{\mathbf{p}_I} K(\mathbf{p}_I, \mathbf{p}_J^1), \quad \frac{d\mathbf{p}_I}{dt} = -\nabla_{\boldsymbol{\theta}_I} U(\boldsymbol{\theta}_I, \boldsymbol{\theta}_J^1) \quad (\text{S6})$$

with the initial condition $\{\boldsymbol{\theta}_I^{1/2}(0), \mathbf{p}_I^{1/2}(0)\} = (\boldsymbol{\theta}_I^{1/2}, \mathbf{p}_I^{1/2})$. By the energy-preserving property of (exact) Hamiltonian dynamics, (S4) becomes

$$\begin{aligned} H(\boldsymbol{\theta}^1, \mathbf{p}^1) - H(\boldsymbol{\theta}^0, \mathbf{p}^0) \\ = H(\boldsymbol{\theta}^1, \mathbf{p}^1) - H\{\boldsymbol{\theta}_I^{1/2}(\epsilon/2), \boldsymbol{\theta}_J^1, \mathbf{p}_I^{1/2}(\epsilon/2), \mathbf{p}_J^1\} \\ + H(\boldsymbol{\theta}_I^{1/2}, \boldsymbol{\theta}_J^0, \mathbf{p}_I^{1/2}, \mathbf{p}_J^0) - H\{\boldsymbol{\theta}_I^0(\epsilon/2), \boldsymbol{\theta}_J^0, \mathbf{p}^0(\epsilon/2), \mathbf{p}_J^0\} \end{aligned} \quad (\text{S7})$$

In essence, (S7) says that the error in Hamiltonian comes only from the numerical approximation errors in solving the differential equations (S5) and (S6). Lemma A2 below quantifies such errors and its results

can be related to the error in Hamiltonian by observing that

$$\begin{aligned}
& H(\boldsymbol{\theta}_I^{1/2}, \boldsymbol{\theta}_J^0, \mathbf{p}_I^{1/2}, \mathbf{p}_J^0) - H\{\boldsymbol{\theta}_I^0(\epsilon/2), \boldsymbol{\theta}_J^0, \mathbf{p}_I^0(\epsilon/2), \mathbf{p}_J^0\} \\
&= U(\boldsymbol{\theta}_I^{1/2}, \boldsymbol{\theta}_J^0) - U\{\boldsymbol{\theta}_I^0(\epsilon/2), \boldsymbol{\theta}_J^0\} + K(\mathbf{p}_I^{1/2}, \mathbf{p}_J^0) - K\{\mathbf{p}_I^0(\epsilon/2), \mathbf{p}_J^0\} \\
&= \nabla_{\boldsymbol{\theta}_I}^\top U(\boldsymbol{\theta}_I^{1/2}, \boldsymbol{\theta}_J^0)\{\boldsymbol{\theta}_I^{1/2} - \boldsymbol{\theta}_I^0(\epsilon/2)\} + \nabla_{\mathbf{p}_I}^\top K(\mathbf{p}_I^{1/2}, \mathbf{p}_J^0)\{\mathbf{p}_I^{1/2} - \mathbf{p}_I^0(\epsilon/2)\} \\
&\quad + O\{\|\boldsymbol{\theta}_I^{1/2} - \boldsymbol{\theta}_I(\epsilon/2)\|^2\} + O\{\|\mathbf{p}_I^{1/2} - \mathbf{p}_I(\epsilon/2)\|^2\}
\end{aligned} \tag{S8}$$

Now applying (S13) of Lemma A2 with $\tilde{\epsilon} = \epsilon/2$, $(\boldsymbol{\theta}_I, \mathbf{p}_I) = (\boldsymbol{\theta}_I^0, \mathbf{p}_I^0)$, and $(\boldsymbol{\theta}_I^*, \mathbf{p}_I^*) = (\boldsymbol{\theta}_I^{1/2}, \mathbf{p}_I^{1/2})$, we obtain

$$\begin{aligned}
& H(\boldsymbol{\theta}_I^{1/2}, \boldsymbol{\theta}_J^0, \mathbf{p}_I^{1/2}, \mathbf{p}_J^0) - H\{\boldsymbol{\theta}_I^0(\epsilon/2), \boldsymbol{\theta}_J^0, \mathbf{p}_I^0(\epsilon/2), \mathbf{p}_J^0\} \\
&= -\frac{\epsilon^2}{8} \nabla_{\boldsymbol{\theta}_I}^\top U(\boldsymbol{\theta}_I^{1/2}, \boldsymbol{\theta}_J^0) \mathcal{I}_K(\mathbf{p}_I^{1/2}, \mathbf{p}_J^0) \nabla_{\boldsymbol{\theta}_I} U(\boldsymbol{\theta}_I^{1/2}, \boldsymbol{\theta}_J^0) \\
&\quad + \frac{\epsilon^2}{8} \nabla_{\mathbf{p}_I}^\top K(\mathbf{p}_I^{1/2}, \mathbf{p}_J^0) \mathcal{I}_U(\boldsymbol{\theta}_I^{1/2}, \boldsymbol{\theta}_J^0) \nabla_{\mathbf{p}_I} K(\mathbf{p}_I^{1/2}, \mathbf{p}_J^0) + O(\epsilon^3)
\end{aligned} \tag{S9}$$

In a similar manner, it follows from (S15) of Lemma A2 that

$$\begin{aligned}
& H(\boldsymbol{\theta}_I^1, \boldsymbol{\theta}_J^1, \mathbf{p}_I^1, \mathbf{p}_J^1) - H\{\boldsymbol{\theta}_I^{1/2}(\epsilon/2), \boldsymbol{\theta}_J^1, \mathbf{p}_I^{1/2}(\epsilon/2), \mathbf{p}_J^1\} f \\
&= \frac{\epsilon^2}{8} \nabla_{\boldsymbol{\theta}_I}^\top U(\boldsymbol{\theta}_I^1, \boldsymbol{\theta}_J^1) \mathcal{I}_K(\mathbf{p}_I^{1/2}, \mathbf{p}_J^1) \nabla_{\boldsymbol{\theta}_I} U(\boldsymbol{\theta}_I^{1/2}, \boldsymbol{\theta}_J^1) \\
&\quad - \frac{\epsilon^2}{8} \nabla_{\mathbf{p}_I}^\top K(\mathbf{p}_I^1, \mathbf{p}_J^1) \mathcal{I}_U(\boldsymbol{\theta}_I^{1/2}, \boldsymbol{\theta}_J^1) \nabla_{\mathbf{p}_I} K(\mathbf{p}_I^{1/2}, \mathbf{p}_J^1) + O(\epsilon^3) \\
&= \frac{\epsilon^2}{8} \nabla_{\boldsymbol{\theta}_I}^\top U(\boldsymbol{\theta}_I^{1/2}, \boldsymbol{\theta}_J^1) \mathcal{I}_K(\mathbf{p}_I^{1/2}, \mathbf{p}_J^1) \nabla_{\boldsymbol{\theta}_I} U(\boldsymbol{\theta}_I^{1/2}, \boldsymbol{\theta}_J^1) \\
&\quad - \frac{\epsilon^2}{8} \nabla_{\mathbf{p}_I}^\top K(\mathbf{p}_I^{1/2}, \mathbf{p}_J^1) \mathcal{I}_U(\boldsymbol{\theta}_I^{1/2}, \boldsymbol{\theta}_J^1) \nabla_{\mathbf{p}_I} K(\mathbf{p}_I^{1/2}, \mathbf{p}_J^1) + O(\epsilon^3)
\end{aligned} \tag{S10}$$

The result (S1) now follows by simply noting that the derivatives of K with respect to \mathbf{p}_I are independent of \mathbf{p}_J . \square

LEMMA A2. For $(\boldsymbol{\theta}_J, \mathbf{p}_J)$ fixed, let $\{\boldsymbol{\theta}_I(t), \mathbf{p}_I(t)\}$ denote the solution of the differential equation

$$\frac{d\boldsymbol{\theta}_I}{dt} = \nabla_{\mathbf{p}_I} K(\mathbf{p}_I, \mathbf{p}_J), \quad \frac{d\mathbf{p}_I}{dt} = -\nabla_{\boldsymbol{\theta}_I} U(\boldsymbol{\theta}_I, \boldsymbol{\theta}_J) \tag{S11}$$

with the initial condition $(\boldsymbol{\theta}_I(0), \mathbf{p}_I(0)) = (\boldsymbol{\theta}_I, \mathbf{p}_I)$. The approximation error of the numerical scheme

$$\boldsymbol{\theta}_I^* = \boldsymbol{\theta}_I + \tilde{\epsilon} \nabla_{\mathbf{p}_I} K(\mathbf{p}_I^*, \mathbf{p}_J), \quad \mathbf{p}_I^* = \mathbf{p}_I - \tilde{\epsilon} \nabla_{\boldsymbol{\theta}_I} U(\boldsymbol{\theta}_I, \boldsymbol{\theta}_J) \tag{S12}$$

satisfies

$$\begin{aligned}
\boldsymbol{\theta}_I^* - \boldsymbol{\theta}_I(\tilde{\epsilon}) &= -\frac{\tilde{\epsilon}^2}{2} \mathcal{I}_K(\mathbf{p}_I^*, \mathbf{p}_J) \nabla_{\boldsymbol{\theta}_I} U(\boldsymbol{\theta}_I^*, \boldsymbol{\theta}_J) + O(\tilde{\epsilon}^3) \\
\mathbf{p}_I^* - \mathbf{p}_I(\tilde{\epsilon}) &= \frac{\tilde{\epsilon}^2}{2} \mathcal{I}_U(\boldsymbol{\theta}_I^*, \boldsymbol{\theta}_J) \nabla_{\mathbf{p}_I} K(\mathbf{p}_I^*, \mathbf{p}_J) + O(\tilde{\epsilon}^3)
\end{aligned} \tag{S13}$$

where $\mathcal{I}_U = \partial^2 U / \partial \boldsymbol{\theta}_I^2$ and $\mathcal{I}_K = \partial^2 K / \partial \mathbf{p}_I^2$ are the Hessians of U and K with respect to $\boldsymbol{\theta}_I$ and \mathbf{p}_I . Similarly, the approximation error of the numerical scheme

$$\boldsymbol{\theta}_I^* = \boldsymbol{\theta}_I + \tilde{\epsilon} \nabla_{\mathbf{p}_I} K(\mathbf{p}_I, \mathbf{p}_J), \quad \mathbf{p}_I^* = \mathbf{p}_I - \tilde{\epsilon} \nabla_{\boldsymbol{\theta}_I} U(\boldsymbol{\theta}_I^*, \boldsymbol{\theta}_J) \tag{S14}$$

satisfies

$$\begin{aligned}
\boldsymbol{\theta}_I^* - \boldsymbol{\theta}_I(\tilde{\epsilon}) &= \frac{\tilde{\epsilon}^2}{2} \mathcal{I}_K(\mathbf{p}_I, \mathbf{p}_J) \nabla_{\boldsymbol{\theta}_I} U(\boldsymbol{\theta}_I, \boldsymbol{\theta}_J) + O(\tilde{\epsilon}^3) \\
\mathbf{p}_I^* - \mathbf{p}_I(\tilde{\epsilon}) &= -\frac{\tilde{\epsilon}^2}{2} \mathcal{I}_U(\boldsymbol{\theta}_I, \boldsymbol{\theta}_J) \nabla_{\mathbf{p}_I} K(\mathbf{p}_I, \mathbf{p}_J) + O(\tilde{\epsilon}^3)
\end{aligned} \tag{S15}$$

Proof. The proofs of (S13) and (S15) are very similar, so we focus on the derivations of (S13). The Taylor expansion of $\boldsymbol{\theta}_I(t)$ yields

$$\begin{aligned}\boldsymbol{\theta}_I(\tilde{\epsilon}) - \boldsymbol{\theta}_I &= \tilde{\epsilon} \frac{d\boldsymbol{\theta}}{dt} + \frac{\tilde{\epsilon}^2}{2} \frac{d^2\boldsymbol{\theta}}{dt^2} + O(\tilde{\epsilon}^3) \\ &= \tilde{\epsilon} \nabla_{\mathbf{p}_I} K(\mathbf{p}_I, \mathbf{p}_J) - \frac{\tilde{\epsilon}^2}{2} \mathcal{I}_K(\mathbf{p}_I, \mathbf{p}_J) \nabla_{\boldsymbol{\theta}_I} U(\boldsymbol{\theta}_I, \boldsymbol{\theta}_J) + O(\tilde{\epsilon}^3)\end{aligned}\tag{S16}$$

On the other hand, the Taylor expansion of $\nabla_{\mathbf{p}_I} K(\mathbf{p}_I^*, \mathbf{p}_J)$ in the first variable yields

$$\begin{aligned}\boldsymbol{\theta}_I^* - \boldsymbol{\theta}_I &= \tilde{\epsilon} \nabla_{\mathbf{p}_I} K(\mathbf{p}_I, \mathbf{p}_J) + \tilde{\epsilon} \mathcal{I}_K(\mathbf{p}_I, \mathbf{p}_J) (\mathbf{p}_I^* - \mathbf{p}_I) + \tilde{\epsilon} O(\|\mathbf{p}_I^* - \mathbf{p}_I\|^2) \\ &= \tilde{\epsilon} \nabla_{\mathbf{p}_I} K(\mathbf{p}_I, \mathbf{p}_J) - \tilde{\epsilon}^2 \mathcal{I}_K(\mathbf{p}_I, \mathbf{p}_J) \nabla_{\boldsymbol{\theta}_I} U(\boldsymbol{\theta}_I, \boldsymbol{\theta}_J) + O(\tilde{\epsilon}^3)\end{aligned}\tag{S17}$$

Subtracting (S16) from (S17), we obtain

$$\begin{aligned}\boldsymbol{\theta}_I^* - \boldsymbol{\theta}_I(\tilde{\epsilon}) &= -\frac{\tilde{\epsilon}^2}{2} \mathcal{I}_K(\mathbf{p}_I, \mathbf{p}_J) \nabla_{\boldsymbol{\theta}_I} U(\boldsymbol{\theta}_I, \boldsymbol{\theta}_J) + O(\tilde{\epsilon}^3) \\ &= -\frac{\tilde{\epsilon}^2}{2} \mathcal{I}_K(\mathbf{p}_I^*, \mathbf{p}_J) \nabla_{\boldsymbol{\theta}_I} U(\boldsymbol{\theta}_I^*, \boldsymbol{\theta}_J) + O(\tilde{\epsilon}^3)\end{aligned}\tag{S18}$$

where the second equality again follows from a Taylor expansion applied to the leading order term. The error estimate for the momentum variable is similar; the Taylor expansion of $\mathbf{p}_I(t)$ gives

$$\mathbf{p}_I(\tilde{\epsilon}) - \mathbf{p}_I = -\tilde{\epsilon} \nabla_{\boldsymbol{\theta}_I} U(\boldsymbol{\theta}_I, \boldsymbol{\theta}_J) - \frac{\tilde{\epsilon}^2}{2} \mathcal{I}_U(\boldsymbol{\theta}_I, \boldsymbol{\theta}_J) \nabla_{\mathbf{p}_I} K(\mathbf{p}_I, \mathbf{p}_J) + O(\tilde{\epsilon}^3)\tag{S19}$$

Subtracting (S19) from (S12), we obtain

$$\begin{aligned}\mathbf{p}_I^* - \mathbf{p}_I(\tilde{\epsilon}) &= \frac{\tilde{\epsilon}^2}{2} \mathcal{I}_U(\boldsymbol{\theta}_I, \boldsymbol{\theta}_J) \nabla_{\mathbf{p}_I} K(\mathbf{p}_I, \mathbf{p}_J) + O(\tilde{\epsilon}^3) \\ &= \frac{\tilde{\epsilon}^2}{2} \mathcal{I}_U(\boldsymbol{\theta}_I^*, \boldsymbol{\theta}_J) \nabla_{\mathbf{p}_I} K(\mathbf{p}_I^*, \mathbf{p}_J) + O(\tilde{\epsilon}^3)\end{aligned}\tag{S20}$$

S8.2. Global error in Hamiltonian

Theorem A2 below establishes the global error in Hamiltonian to be $O(\epsilon^2)$. For its proof, we recall that Algorithm 2 is designed under the assumption that the parameter space has a partition $\mathbb{R}^{|I|} \times \mathbb{R}^{|J|} = \cup_k \mathbb{R}^{|I|} \times \Omega_k$ such that $U(\boldsymbol{\theta})$ is smooth on $\mathbb{R}^{|I|} \times \Omega_k$ for each k . Below, in relating the local error to the global one, we make the dependence of a numerical solution on a stepsize ϵ explicit and denote the value of a numerical solution after ℓ steps by $(\boldsymbol{\theta}_\epsilon^\ell, \mathbf{p}_\epsilon^\ell)$.

THEOREM A2. *Suppose that each Ω_k is rectangular i.e. its boundary consists of planes perpendicular to one of the coordinates of $\boldsymbol{\theta}_J$. Then the global error $H(\boldsymbol{\theta}_\epsilon^L, \mathbf{p}_\epsilon^L) - H(\boldsymbol{\theta}^0, \mathbf{p}^0)$ with $L = L(\epsilon) = \lfloor \tau/\epsilon \rfloor$ incurred by Algorithm 2 is of order $O(\epsilon^2 D)$ where D is the number of discontinuities in U encountered along the trajectory $\{\boldsymbol{\theta}(t), 0 \leq t \leq \tau\}$.*

The assumption stated in Theorem A2 is required for our proof of Theorem A3 and is satisfied whenever the discontinuous target π is obtained by the embedding of discrete parameters described in Section 2.2. We however believe the order of the global error to remain unchanged under more general conditions.

Proof. The global error is given as a sum of the local errors:

$$H(\boldsymbol{\theta}_\epsilon^L, \mathbf{p}_\epsilon^L) - H(\boldsymbol{\theta}^0, \mathbf{p}^0) = \sum_{\ell=1}^L \{H(\boldsymbol{\theta}_\epsilon^\ell, \mathbf{p}_\epsilon^\ell) - H(\boldsymbol{\theta}_\epsilon^{\ell-1}, \mathbf{p}_\epsilon^{\ell-1})\}\tag{S21}$$

Let $D(\epsilon)$ denote the size of the set \mathcal{D}_ϵ as defined below:

$$\mathcal{D}_\epsilon = \left\{ \ell \in \{1, \dots, L\} : \right. \\ \left. \boldsymbol{\theta}_{\epsilon, J}^\ell \text{ and } \boldsymbol{\theta}_{\epsilon, J}^{\ell-1} \text{ belong to two separate regions of the partition } \Omega_k \text{'s} \right\} \quad (\text{S22})$$

By the result of Corollary A1, we know that the local error is $O(\epsilon^2)$ if $\ell \in \mathcal{D}_\epsilon$ and of $O(\epsilon^3)$ otherwise. Therefore, (S21) is a sum of $D(\epsilon)$ terms of $O(\epsilon^2)$ errors and $L(\epsilon) - D(\epsilon)$ terms of $O(\epsilon^3)$ errors, yielding the global error of $O\{D(\epsilon)\epsilon^2\}$. To complete the proof, it follows from Theorem A3 that $D(\epsilon)$ as $\epsilon \rightarrow 0$ converges to the number of discontinuities in U encountered along the trajectory $\{\boldsymbol{\theta}(t), 0 \leq t \leq \tau\}$. \square

THEOREM A3. *Under the assumption of Theorem A2, we have*

$$\sup_{\ell=1, \dots, L(\epsilon)} \left\| \{\boldsymbol{\theta}(\ell\epsilon), \mathbf{p}(\ell\epsilon)\} - (\boldsymbol{\theta}_\epsilon^\ell, \mathbf{p}_\epsilon^\ell) \right\| = O(\epsilon) \quad (\text{S23})$$

Proof. First note that the trajectory of Hamiltonian dynamics corresponding to the kinetic energy (17) can be partitioned into \tilde{D} segments $\{\boldsymbol{\theta}(t) : t_m < t < t_{m+1}\}_m$ for $0 = t_0 < t_1 < \dots < t_{\tilde{D}} = \tau$ so that on each segment $d\boldsymbol{\theta}_J/dt = \mathbf{m}_J^{-1} \odot \text{sign}(\mathbf{p}_J)$ is constant.

The numerical solution approximate the exact solution $\boldsymbol{\theta}(t) \rightarrow \boldsymbol{\theta}(t + \ell\epsilon)$ up to an error of $O(\epsilon^2)$ for any ℓ provided that $\boldsymbol{\theta}(t)$ and $\boldsymbol{\theta}(t + \ell\epsilon)$ belongs to the same segment $\{\boldsymbol{\theta}(t) : t_m < t < t_{m+1}\}$. This is for the following reason. For all sufficiently small ϵ , the coordinate-wise updates of discontinuous parameters yield the exact solution to

$$\frac{d\boldsymbol{\theta}_J}{dt} = \mathbf{m}_J^{-1} \odot \text{sign}(\mathbf{p}_J), \quad \frac{d\mathbf{p}_J}{dt} = -\nabla_{\boldsymbol{\theta}_J} U(\boldsymbol{\theta}), \quad \frac{d\boldsymbol{\theta}_{-J}}{dt} = \frac{d\mathbf{p}_{-J}}{dt} = \mathbf{0} \quad (\text{S24})$$

provided no sign change in \mathbf{p}_J is encountered. In this case, Algorithm 2 coincides with a symmetric splitting of Hamilton's equation in which the individual components are solved exactly and hence the numerical approximation of $\boldsymbol{\theta}(t) \rightarrow \boldsymbol{\theta}(t + \epsilon)$ locally agrees with the exact solution up to an error of $O(\epsilon^3)$ (Leimkuhler & Reich, 2005).

Now consider the case when $\boldsymbol{\theta}(t)$ and $\boldsymbol{\theta}(t + \epsilon)$ do not belong to the same segment. In this case, the coordinate-wise integrator approximates the change in $d\boldsymbol{\theta}_J/dt$ through the momentum flip $p_j \rightarrow -p_j$ for an appropriate j while θ_j held fixed. This may or may not be caused by a discontinuity in U along the path $\{\boldsymbol{\theta}(s) : t < s < t + \epsilon\}$. When there is no discontinuity, the approximation is always accurate up to an error of $O(\epsilon)$. When there is a discontinuity, our assumption on the boundaries of Ω_k 's guarantees the numerical approximation error to be $O(\epsilon)$.

To summarize, we have shown that the total accumulated error is $O(\epsilon^2)$ while the solution stays within the same segment $\{\boldsymbol{\theta}(t) : t_m < t < t_{m+1}\}_m$ and then an additional error of $O(\epsilon)$ is incurred when crossing from one segment to another. Since the solution trajectory consists of \tilde{D} such segments, the total accumulated error is $O\{\tilde{D}(\epsilon + \epsilon^2)\} = O(\tilde{D}\epsilon)$. \square